

This work was written as part of one of the author's official duties as an Employee of the United States Government and is therefore a work of the United States Government. In accordance with 17 U.S.C. 105, no copyright protection is available for such works under U.S. Law.

Public Domain Mark 1.0

<https://creativecommons.org/publicdomain/mark/1.0/>

Access to this work was provided by the University of Maryland, Baltimore County (UMBC) ScholarWorks@UMBC digital repository on the Maryland Shared Open Access (MD-SOAR) platform.

**Please provide feedback**

Please support the ScholarWorks@UMBC repository by emailing [scholarworks-group@umbc.edu](mailto:scholarworks-group@umbc.edu) and telling us what having access to this work means to you and why it's important to you. Thank you.

# Multiangle Imaging SpectroRadiometer global aerosol product assessment by comparison with the Aerosol Robotic Network

Ralph A. Kahn,<sup>1</sup> Barbara J. Gaitley,<sup>2</sup> Michael J. Garay,<sup>3</sup> David J. Diner,<sup>2</sup> Thomas F. Eck,<sup>4</sup> Alexander Smirnov,<sup>5</sup> and Brent N. Holben<sup>1</sup>

Received 28 June 2010; revised 4 August 2010; accepted 11 August 2010; published 7 December 2010.

[1] A statistical approach is used to assess the quality of the Multiangle Imaging SpectroRadiometer (MISR) version 22 (V22) aerosol products. Aerosol optical depth (AOD) retrieval results are improved relative to the early postlaunch values reported by [Kahn *et al.* (2005)], which varied with particle type category. Overall, about 70% to 75% of MISR AOD retrievals fall within 0.05 or  $20\% \times \text{AOD}$  of the paired validation data from the Aerosol Robotic Network (AERONET), and about 50% to 55% are within 0.03 or  $10\% \times \text{AERONET AOD}$ , except at sites where dust or mixed dust and smoke are commonly found. Retrieved particle microphysical properties amount to categorical values, such as three size groupings: “small,” “medium,” and “large.” For particle size, ground-based AERONET sun photometer Angstrom exponents are used to assess statistically the corresponding MISR values, which are interpreted in terms of retrieved size categories. Coincident single-scattering albedo (SSA) and fraction AOD spherical data are too limited for statistical validation. V22 distinguishes two or three size bins, depending on aerosol type, and about two bins in SSA (absorbing vs. nonabsorbing), as well as spherical vs. nonspherical particles, under good retrieval conditions. Particle type sensitivity varies considerably with conditions and is diminished for midvisible AODs below about 0.15 or 0.2. On the basis of these results, specific algorithm upgrades are proposed and are being investigated by the MISR team for possible implementation in future versions of the product.

**Citation:** Kahn, R. A., B. J. Gaitley, M. J. Garay, D. J. Diner, T. F. Eck, A. Smirnov, and B. N. Holben (2010), Multiangle Imaging SpectroRadiometer global aerosol product assessment by comparison with the Aerosol Robotic Network, *J. Geophys. Res.*, 115, D23209, doi:10.1029/2010JD014601.

## 1. Introduction

[2] Since the launch of the NASA Earth Observing System (EOS) satellites, enormous strides have been made in aerosol optical depth (AOD) remote sensing over land and water [e.g., Martonchik *et al.*, 2009; Kahn *et al.*, 2005a; Remer *et al.*, 2005, 2008]. The global data sets produced by the Multiangle Imaging SpectroRadiometer (MISR) and Moderate Resolution Imaging Spectroradiometer (MODIS) instruments have contributed to the reduction in uncertainties in aerosol transport and radiative impact modeling [e.g., Zhang and Christopher, 2003; Kinne *et al.*, 2006; Yu *et al.*, 2006; Kim and Ramanathan, 2008; Chen *et al.*, 2009], leading, for

example, to a reduction in the overall climate forcing uncertainty attributed to aerosols [Haywood and Schulz, 2007; IPCC, 2007].

[3] However, significant further reduction in aerosol climate impact assessment depends on retrieving aerosol type along with AOD. MISR-retrieved aerosol type has been used in a range of applications, including particle shape [Kalashnikova and Kahn, 2006; Liu *et al.*, 2007a, 2007b], and combinations of size distribution and single-scattering albedo (SSA) constraints [Chen *et al.*, 2008], size and shape [Kalashnikova and Kahn, 2008; Dey and Di Girolamo, 2010; Pierce *et al.*, 2010], and all three microphysical property constraints [Kahn *et al.*, 2009b]. In addition to the intrinsic value of such information for helping determine particle composition and origin, and for mapping aerosol transport, deposition, and evolution, particle type is among the key factors determining AOD retrieval accuracy itself [e.g., Kahn *et al.*, 2007a].

[4] MISR was launched into a sun-synchronous polar orbit in December 1999, aboard the NASA EOS Terra satellite. Terra crosses the equator on the descending node at about 1030 local time. MISR is unique among the EOS-era satellite instruments in having a combination of high spatial

<sup>1</sup>Laboratory for Atmospheres, NASA Goddard Space Flight Center, Greenbelt, Maryland, USA.

<sup>2</sup>Jet Propulsion Laboratory, California Institute of Technology, Pasadena, California, USA.

<sup>3</sup>Raytheon Company, Pasadena, California, USA.

<sup>4</sup>Goddard Earth Sciences and Technology Center, University of Maryland Baltimore County, Baltimore, Maryland, USA.

<sup>5</sup>Sigma Space Corporation, Lanham, Maryland, USA.

resolution, a wide range of along-track view angles, and high-accuracy radiometric calibration and stability [Diner *et al.*, 1998]. Global coverage (to  $\pm 82^\circ$  latitude) is obtained about once per week.

[5] MISR measures upwelling short-wave radiance from Earth in four spectral bands, centered at 446, 558, 672, and 866 nm, at each of nine view angles spread out in the forward and aft directions along the flight path, at  $70.5^\circ$ ,  $60.0^\circ$ ,  $45.6^\circ$ ,  $26.1^\circ$ , and nadir. Over a period of 7 min, as the spacecraft flies overhead, a 380 km wide swath of Earth is successively viewed by each of MISR's nine cameras. As a result, the instrument samples a very large range of scattering angles, between about  $60^\circ$  and  $160^\circ$  at midlatitudes, providing information on aerosol microphysical properties. These views also capture air-mass factors ranging from 1 to 3, offering sensitivity to optically thin aerosol layers and allowing aerosol retrieval algorithms to distinguish surface from atmospheric contributions to the top-of-atmosphere (TOA) radiance.

[6] The MISR standard aerosol retrieval algorithm runs in an operational, fully automatic mode. It reports AOD and aerosol type at 17.6 km resolution, by analyzing data from  $16 \times 16$  pixel regions of 1.1 km resolution, MISR TOA radiances [Diner *et al.*, 2006; Kahn *et al.*, 2009a; Martonchik *et al.*, 2009]. Prelaunch studies predicted that MISR sensitivity to AOD and particle properties would vary with conditions. At least over dark water, for good retrieval conditions and AODs at midvisible wavelengths larger than about 0.15, MISR was expected to distinguish about three to five groupings based on particle size, two to four groupings of SSA, and spherical vs. nonspherical particles [Kahn *et al.*, 1997, 1998, 2001]. These studies usually modeled good retrieval conditions over water as a uniform, cloud-free scene, with a dark surface having a near-surface wind speed of about 2.5 m/s; we also tested a range of conditions to assess the robustness of the results.

[7] Using a combination of MISR standard [Martonchik *et al.*, 1998, 2002, 2009] and research [Kahn *et al.*, 2001] aerosol retrieval algorithms, several postlaunch studies focused on MISR sensitivity to particle properties as well as AOD, for individual cases when specific aerosol types dominate. These studies, covering desert dust [Kalashnikova *et al.*, 2005; Kalashnikova and Kahn, 2006; Kahn *et al.*, 2009b], biomass burning [Chen *et al.*, 2008], and cirrus [Pierce *et al.*, 2010] cases, generally confirm prelaunch expectations about size, shape, and SSA sensitivity and add considerable detail to earlier predictions.

[8] Postlaunch statistical assessments of the MISR aerosol products have so far concentrated on AOD [e.g., Diner *et al.*, 2001; Christopher and Wang, 2004; Liu *et al.*, 2004; Martonchik *et al.*, 2004; Abdou *et al.*, 2005; Kahn *et al.*, 2005a; Jiang *et al.*, 2007]. For example, Kahn *et al.* [2005a, hereafter paper 1] evaluated the version 12 (V12) early postlaunch aerosol product by comparing MISR AODs with a 2 year, globally distributed set of AERONET surface-based sun photometer measurements [Holben *et al.*, 1998]. Paper 1 concluded that for V12 of the MISR algorithm, about two thirds of the MISR-retrieved AOD values for which there are coincident AERONET retrievals fall within the larger of 0.05 or  $20\% \times \text{AOD}$  relative to AERONET, and more than a third were within 0.03 or  $10\% \times \text{AOD}$ . The results also suggested that adding more absorbing spherical particles,

more realistic dust optical analogs, and a richer selection of multimodal aerosol mixtures to the algorithm climatology would reduce the remaining AOD discrepancies with AERONET for MISR retrievals over land; in addition, refining instrument low-light-level calibration would reduce or eliminate a small but systematic offset in maritime AOD values.

[9] V22 incorporates many of the suggested upgrades, including a more realistic medium-mode desert dust optical model (see Table 2 [also Kalashnikova *et al.*, 2005]), small to medium, spherical particles having midvisible SSA of 0.8 and 0.9, and more multimodal aerosol distributions in the standard algorithm climatology, along with other algorithm adjustments described in the MISR product documentation (available at [http://eosweb.larc.nasa.gov/PRODOCS/misr/table\\_misr.html](http://eosweb.larc.nasa.gov/PRODOCS/misr/table_misr.html)). In addition, the MISR band-to-band and camera-to-camera radiometric calibration have been improved, which has partly corrected the low-AOD bias relative to AERONET [Diner *et al.*, 2004; Kahn *et al.*, 2005b; Bruegge *et al.*, 2007]. As before, the V22 algorithm reports the best-estimate spectral AODs as “regional mean” values, which are averages, with equal weight, of the AODs obtained in the algorithm climatology for each mixture that passes the acceptance criteria. But the best-estimate particle size, SSA, and fraction AOD spherical are obtained from the aerosol mixture having TOA radiances with the lowest residuals relative to the MISR observations. The AOD associated with the lowest-residual mixture is also reported in the data product. The full MISR data record from February 2000 to the present has been reprocessed to V22.

[10] In this paper we assess the quality of the MISR V22 level 2AS aerosol product over land and water, and make suggestions for additional algorithm refinements. Further assessment and product refinement are justified by the exacting demands on AOD particle-type accuracy for air quality and material transport studies and for evaluation of direct aerosol radiative forcing regionally and globally. The 10 year record is also beginning to make time-series and trend analyses worth pursuing with MISR data. Fortunately, over this period we have acquired much more validation data, which provide better statistics, cover a wider range of environmental conditions, and include more detailed ground-truth measurements than were available early in the MISR mission. In addition, we have learned a great deal from work already done with the MISR products, by the instrument team and many others.

[11] Our approach is to compare the MISR data with coincident observations from 81 globally distributed AERONET sites over 8 years. As in paper 1, we take a statistical approach and stratify the observations by season and expected aerosol type. But here, in addition to comparing the new MISR-retrieved midvisible AODs, we study the Angstrom exponent (ANG) in light of AERONET direct-sun spectral AOD measurements and explore the implications for retrieved particle components and mixtures. These are all total-column effective values, as there is no height-resolved information in either MISR or AERONET aerosol retrievals (though the MISR stereo-product includes aerosol plume heights in wildfire, volcanic, and desert dust near-source regions [Kahn *et al.*, 2007b]). Note also that, as with paper 1, this is not a test of MISR cloud masking, because coincident aerosol retrievals must pass both

## The Data: 81 AERONET Sites with Coincident MISR Observations

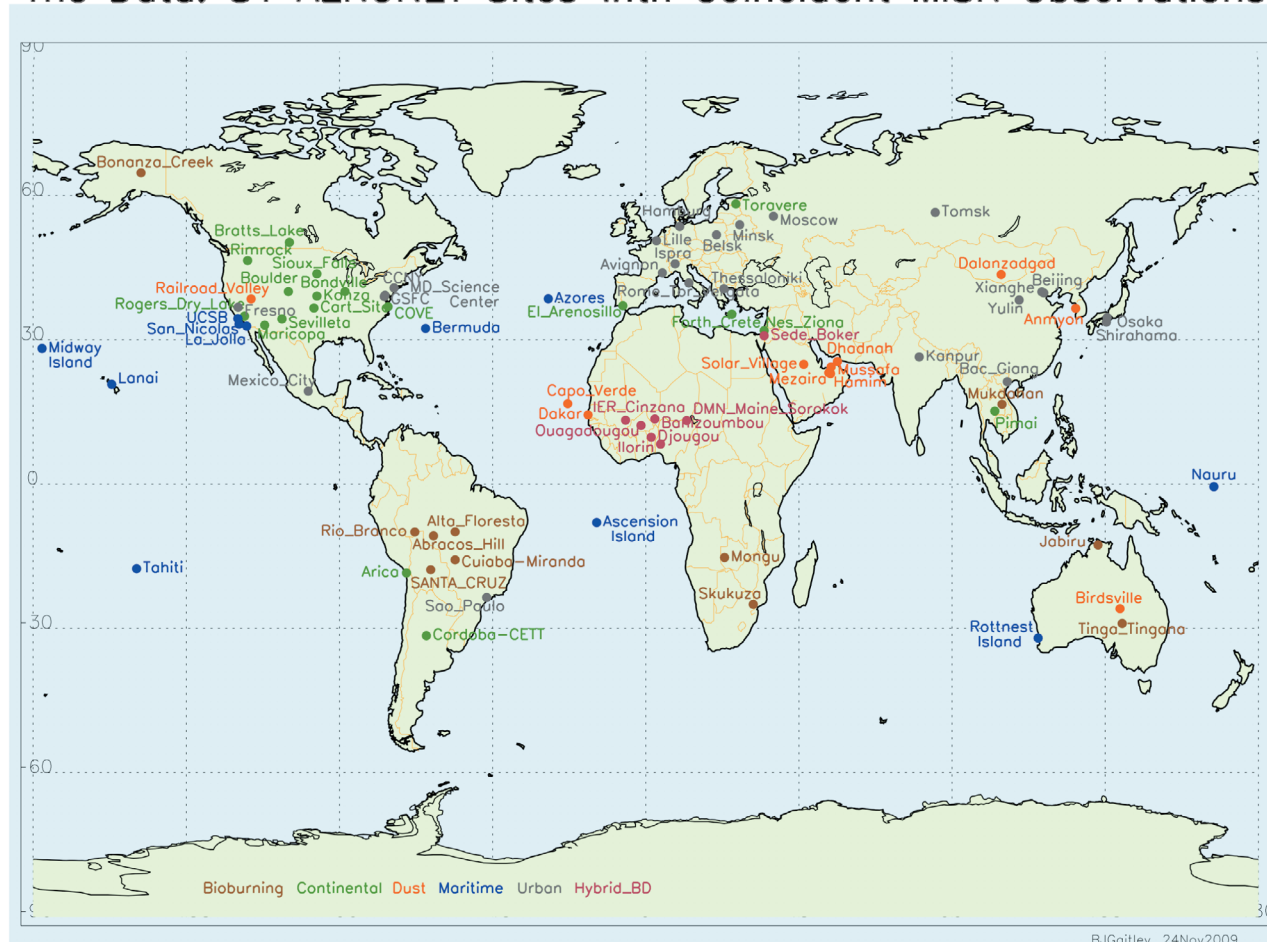


**Figure 1.** Geographical distribution of the 81 sites used in this study. Sites are color-coded according to expected aerosol air mass type: Biomass Burning, brown; Continental, green; Dusty, orange; Maritime, blue; Urban, gray; Hybrid (smoke + dust), red.

the MISR and the AERONET cloud masks to be included in this study. MISR cloud mask performance is the subject of separate studies [e.g., Zhao *et al.*, 2009].

[12] This paper is organized as follows. Section 2 describes how the MISR and AERONET data were selected and processed and gives an overview of sampling statistics. Section 3 summarizes AOD performance; trends and patterns in AOD differences are identified, stratified by location and season so as to separate typical aerosol types, and compared with results from the early postlaunch product studied in paper 1. Section 4 looks in detail at the particle properties reported in the MISR V22 aerosol product, investigates outliers, and explores possible causes for the observed behavior. Section 5 provides a summary of results and recommendations for further product refinements, and the final section presents conclusions.

## 2. Data Selection and Analysis Approach

[13] We compare MISR-retrieved AOD and particle properties with coincident AERONET direct-sun and sky-scan results. The data involved are described in this section.

### 2.1. Aerosol Robotic Network (AERONET) Surface-Based Sun Photometer Network Data

[14] AERONET direct-sun measurements are taken automatically with ground-based CIMEL sun photometers every 15 min during daylight hours. Standard processing includes operational cloud screening [Smirnov *et al.*, 2000] and generates AODs from the direct transmission. AERONET sun photometers are intercalibrated with reference CIMELs, which in turn are calibrated using the Langley method at Mauna Loa Observatory, Hawaii, in bands nominally centered at about 340, 380, 440, 500, 675, 870, and 1020 nm, plus a column water vapor channel [Holben *et al.*, 1998; available at <http://aeronet.gsfc.nasa.gov/>]. For this study we work with V2 AERONET data, at level 2.0. Level 1.5 AERONET AOD data are cloud-screened values, but are calibrated based on a single predeployment comparison with a standard reference, and can have an uncertainty of  $\geq 0.02$ . The level 2 data, for which a second, postdeployment comparison is also used in calibration along with manual validation checks, are somewhat less frequent overall, but they have an AOD measurement accuracy of  $\sim 0.01$  in the mid-visible [Eck *et al.*, 1999]. (We use “midvisible” to represent

**Table 1.** Aeronet Validation Site Locations, Seasonal Coverage, and Multiangle Imaging SpectroRadiometer (MISR) Coincidence Counts<sup>a</sup>

Site Name	Latitude	Longitude	Altitude (m)	DJF	MAM	JJA	SON	Total Observations	Total Seasons
<i>Biomass Burning</i>									
Abracos_Hill	-10.76	-62.36	200	1	3	17	11	32	14
Alta_Floresta	-9.92	-56.02	175	0	4	20	9	33	18
Bonanza_Creek	64.74	-148.32	150	0	15	3	8	26	11
Cuiaba-Miranda	-15.73	-56.02	210	2	8	21	6	37	13
Jabiru	-12.66	132.89	30	6	11	42	27	86	18
Mongu	-15.25	23.15	1107	11	53	63	39	166	30
Mukdahan	16.61	104.68	166	31	14	1	8	54	14
Rio_Branco	-9.96	-67.87	212	1	1	7	7	16	9
Santa_Cruz	-17.80	-63.18	442	6	2	9	2	19	8
Skukuza	-24.99	31.59	150	9	35	50	30	124	30
Tinga_Tingana	-28.98	139.99	38	24	13	15	17	69	19
<i>Continental</i>									
Arica	-18.47	-70.31	25	20	14	2	9	45	15
Bondville	40.05	-88.37	212	18	19	12	27	76	26
BSRN_BAO_Boulder	40.04	-105.01	1604	10	17	53	28	108	27
Bratts_Lake	50.28	-104.70	586	0	12	35	19	66	18
COVE	36.90	-75.71	37	8	21	20	25	74	28
Cart_Site	36.61	-97.49	318	13	19	24	21	77	22
Cordoba-CETT	-31.52	-64.46	730	14	24	28	29	95	21
El_Arenosillo	37.10	-6.73	0	6	5	22	6	39	18
Forth_Crete	35.33	25.28	20	0	5	4	0	9	6
Konza_EDC	39.10	-96.61	341	24	16	41	26	107	26
Maricopa	33.07	-111.97	360	17	30	31	22	100	23
Nes_Ziona	31.92	34.79	40	9	18	32	16	75	23
Pimai	15.18	102.56	220	24	14	3	2	43	12
Rimrock	46.49	-116.99	824	8	10	36	21	75	23
Rogers_Dry_Lake	34.93	-117.89	680	20	53	63	31	167	20
Sevilleta	34.35	-106.89	1477	8	22	39	11	80	24
Sioux_Falls	43.74	-96.63	500	4	11	30	25	70	20
Toravere	58.26	26.46	70	0	16	12	14	42	16
<i>Dusty</i>									
Anmyon	36.54	126.33	47	2	9	5	4	20	13
Birdsville	-25.90	139.35	46	12	4	3	7	26	7
Capo_Verde	16.73	-22.93	60	18	21	18	14	71	27
Dakar	14.39	-16.96	0	20	17	14	20	71	19
Dalanzadgad	43.58	104.42	1470	30	28	15	34	107	27
Dhadnah	25.51	56.33	81	2	13	16	7	38	13
Hamim	22.97	54.30	209	5	15	6	13	39	13
Mezaira	23.15	53.78	204	0	0	9	3	12	3
Mussafa	24.37	54.47	10	6	7	7	10	30	7
Railroad_Valley	38.50	-115.96	1435	16	14	44	47	121	18
Solar_Village	24.91	46.41	650	7	33	59	11	110	25
<i>Maritime</i>									
Ascension_Island	-7.98	-14.41	30	16	5	14	8	43	19
Azores	38.53	-28.63	50	0	2	6	2	10	8
Bermuda	32.37	-64.70	10	0	2	5	3	10	8
La_Jolla	32.87	-117.25	115	10	18	17	11	56	19
Lanai	20.74	-156.92	20	13	16	12	7	48	14
Midway_Island	28.21	-177.38	0	15	7	16	12	50	14
Nauru	-0.52	166.92	7	1	7	1	10	19	10
Rottneat_Island	-32.00	115.30	40	16	17	7	6	46	10
San_Nicolas	33.26	-119.49	133	6	11	5	7	29	16
Tahiti	-17.58	-149.61	98	2	7	9	7	25	13
UCSB	34.42	-119.85	33	11	8	7	16	42	12
<i>Urban</i>									
Avignon	43.93	4.88	32	34	44	65	41	184	30
Bac_Giang	21.29	106.23	15	4	3	1	10	18	9
Beijing	39.98	116.38	92	25	33	25	32	115	24
Belsk	51.84	20.79	190	0	7	10	7	24	14
CCNY	40.82	-73.95	100	11	12	10	18	51	21
Fresno	36.78	-19.77	110	10	24	46	37	117	23
GSFC	38.99	-76.84	87	31	38	7	40	116	29
Hamburg	53.57	9.97	105	6	20	12	22	60	19
Ispra	45.80	8.63	235	1	17	17	10	45	22
Kanpur	26.45	80.35	142	23	33	10	31	97	25

**Table 1.** (continued)

Site Name	Latitude	Longitude	Altitude (m)	DJF	MAM	JJA	SON	Total Observations	Total Seasons
Lille	50.61	3.14	60	5	12	13	9	39	21
MD_Science_Center	39.28	-76.72	15	11	30	14	35	90	29
Mexico_City	19.33	-99.18	2268	20	26	5	5	56	19
Minsk	53.00	27.50	200	0	6	3	10	19	11
Moscow_MSU_MO	55.70	37.51	192	0	21	9	17	47	17
Osaka	34.65	135.59	50	5	11	1	4	21	17
Rome_Tor_Vergata	41.84	12.65	130	28	25	49	40	142	25
Sao_Paulo	-23.56	-46.74	865	9	11	24	24	68	24
Shirahama	33.69	135.36	10	3	5	5	0	13	11
Thessaloniki	40.63	22.96	60	6	9	9	8	32	10
Tomsk	56.48	85.05	130	0	7	12	13	32	15
XiangHe	39.75	116.96	36	23	21	12	31	87	15
Yulin	38.28	109.72	1080	0	9	7	9	25	6
<i>Hybrid_BD</i>									
Banizoumbou	13.54	2.66	250	50	29	20	45	144	28
DMN_Maine_Sorokok	13.22	12.02	350	19	10	4	9	42	9
Djougou	9.76	1.60	400	14	9	1	7	31	12
IER_Cinzana	13.28	-5.93	285	39	27	18	33	117	15
Ilorin	8.32	4.34	350	20	11	0	5	36	15
Ouagadougou	12.20	-1.40	290	20	11	0	17	67	21
Sede_Boker	30.85	34.78	480	22	48	62	56	188	32

<sup>a</sup>DJF, December–January–February; MAM, March–April–May; JJA, June–July–August; SON, September–October–November.

green-band values, near the peak of the solar spectrum. In the case of MISR specifically, this is band 2, at a 558 nm effective wavelength.) Unlike paper 1, here we include cases for which midvisible AOD values exceed 1.0, in part to take advantage of increased AERONET particle property retrieval accuracy. However, such cases are relatively rare in the coincident data set and often involve dust or smoke plumes having considerable spatial variability; this exacerbates sampling differences and reduces the utility of the comparison for MISR retrieval validation (see paper 1). We also include comparisons between MISR AOD and coincident measurements from AERONET's ship-based Marine Aerosol Network (MAN) sun photometers [Smirnov *et al.*, 2009]. These observations are obtained with handheld Microtops instruments; the data are processed similarly to the CIMEL direct-sun measurements but have the slightly reduced measurement accuracy of  $\sim 0.02$ . The MAN provides additional dark-ocean AOD and ANG cases, which are especially valuable here because there are very few MISR-AERONET coincidences in these situations.

[15] The ANG is derived from the spectral AOD values. It is defined as the negative slope of the least-squares linear fit of  $\ln(\text{AOD})$  vs.  $\ln(\text{wavelength})$ . The ANG is a single variable related to the particle size distribution, though its interpretation is complicated, in part when nonlinearity in spectral AOD dependence is significant and, especially, when multimodal aerosol distributions are present [e.g., Schuster *et al.*, 2006]. AERONET AOD and ANG are both derived solely from direct-sun extinction measurements; as such, the primary uncertainty in these values compared to MISR observations arises from sampling differences, though these can be considerable, especially near aerosol sources, where particle concentrations can vary greatly. Other uncertainties include differences in the wavelengths measured by each instrument, and for the ANG, the fact that it is derived from the slope of multiple observations, each having its own measurement errors.

[16] To facilitate comparisons, note that unlike the linear interpolation applied in paper 1, all AERONET AOD values used in this paper were interpolated to the MISR band effective wavelengths using a second-order polynomial fit to  $\ln(\text{AOD})$  vs.  $\ln(\text{wavelength})$ , as recommended by Eck *et al.* [1999]. As before, the AERONET ANGs are calculated from the spectrally interpolated and temporally averaged direct-sun AERONET AOD values at the four MISR wavelengths, using the same least-squares fitting approach adopted for the MISR data themselves.

[17] AERONET instruments also perform sky scans in the principal plane and across the almucantar at 440, 675, 870, and 1020 nm about once per hour, from which aerosol size distributions and complex refractive indexes are derived [Dubovik and King, 2000; Dubovik *et al.*, 2006]. Retrieved size is reported as a relative, volume-weighted quantity in 22 bins of particle radius, spread logarithmically between 0.05 and 15  $\mu\text{m}$ . Size distributions are also provided in the AERONET standard product as one medium-mode and one coarse-mode log-normal parameter, fit to the 22 bin histogram [Dubovik and King, 2000]. A combination of direct-sun and sky-scan data is used to retrieve spectral indexes of refraction and SSA, though they are considered of high quality only when the solar zenith angle is greater than  $50^\circ$  and the AOD at 440 nm is 0.4 or above [Dubovik *et al.*, 2000].

[18] Figure 1 shows the locations of the 81 AERONET sites used in this study. These sites were selected for their geographic diversity and for their provision of generally good-quality and well-populated data records during the analysis period (Table 1). The sites are classified as Dusty, Biomass Burning, Continental, Urban, Maritime, or Hybrid (smoke + dust), based on the expected dominant aerosol type, at least during some seasons. (Independent, event-by-event classification of aerosol type is possible only on rare occasions, primarily when in situ measurements from field campaigns are available or when major smoke or dust

plumes fall within the coincident MISR-AERONET sampling region.) Although component-particle microphysical properties vary within each category, these six groupings represent broad classes of aerosol air-mass types we expect to distinguish globally with MISR [Kahn *et al.*, 2001], and to some extent, they represent different passive remote-sensing retrieval challenges. But note that these designations are approximate. For example, the Continental category can include, to varying degrees, mixtures of spherical biogenic or combustion particles along with nonspherical soil dust. As a result, care is taken not to overinterpret the differences among categories.

## 2.2. Multiangle Imaging SpectroRadiometer (MISR) Data Attributes and Collocation with Surface Stations

[19] The MISR standard aerosol retrieval algorithm searches a database of TOA radiances simulated for the MISR channels, solar position, and viewing geometries, assuming a range of candidate aerosol mixtures and optical depths, and compares them with the observed radiances [Martonchik *et al.*, 1998, 2009]. Component-particle optical properties assumed in the algorithm cover ranges of “small,” “medium,” and “large,” nonabsorbing and absorbing, and spherical and randomly oriented nonspherical types (Table 2). A limited selection of mixtures of these components is used in the V22 algorithm, as listed in Table 3. The entries are organized so that, for most of Table 3, each decade contains mixtures among a fixed set of components, in systematically varying proportions. Exclusively spherical, nonabsorbing components are found in mixtures 1 to 30, with the fine-mode components having progressively larger sizes for mixtures 1–10, 11–20, and 21–30. Mixtures 31–40 and 41–50 include spherical, absorbing fine-mode components, with midvisible SSAs of 0.90 and 0.80, respectively, and 51–74 are mixtures that contain nonspherical medium- and coarse-mode dust optical analogs. Overall sensitivity to particle-type AOD fraction is about 0.2 for total column AOD  $\geq 0.15$  and diminishes for lower AODs [Chen *et al.*, 2008; Kalashnikova and Kahn, 2006].

[20] Aerosol retrieval success is measured by the degree to which observed multiangle, multispectral TOA radiances match modeled radiances, using several chi-square criteria [e.g., Kahn *et al.*, 1998; Martonchik *et al.*, 1998, 2009]. In V22 the MISR ANG is obtained from the mean optical depths of all successful mixtures, calculated separately at each MISR wavelength. As with the AERONET data, the MISR aerosol retrievals used here meet the cloud-free and other high-data-quality standards set by the experiment teams [e.g., Diner *et al.*, 2006; Kahn *et al.*, 2009a; summarized in the MISR Data Quality Statement distributed online with MISR data products; available at [http://eosweb.larc.nasa.gov/PRODOCS/misr/table\\_misr.html](http://eosweb.larc.nasa.gov/PRODOCS/misr/table_misr.html)]. MISR level 2 aerosol retrievals use only data that pass angle-to-angle smoothness and spatial correlation tests [Martonchik *et al.*, 2002], as well as stereoscopically derived cloud masks and adaptive cloud-screening brightness thresholds [Di Girolamo and Wilson, 2003; Zhao and Di Girolamo, 2004].

[21] As in paper 1, we searched the V22 product for overflights having successful retrievals either in the MISR 17.6 km retrieval region containing each AERONET station selected (the “central” region) or in one or more of the eight retrieval regions surrounding the central one. We use both

the central and all available surrounding region retrievals for comparison with AERONET AODs; values obtained for the surrounding regions help assess AOD spatial variability on 20 to 50 km scales. We also required in paper 1 that the AERONET time series for each coincidence included at least one AOD measurement during the hour before the MISR overpass and at least one during the hour after the overpass. We do the same here.

[22] A fundamental difference between MISR and AERONET AOD observations is that MISR acquires instantaneous data over an entire 20 to 50 km study area (one central plus eight surrounding 17.6 km retrieval regions), whereas AERONET obtains a time series of point data at each surface station. For each event we averaged with equal weight all available AERONET AOD retrievals for a 2 h window centered on the MISR overpass time. This crudely covers the period during which aerosols advecting at 5 to 15 m/s would traverse the MISR study area, though not necessarily sampling it uniformly. We rely on the large number of events included in this study to average out any subtle sampling anomalies, and we highlight as outliers any individual pathological cases. We also take the likely limitations of these assumptions into consideration when drawing conclusions.

[23] There are far fewer once-hourly AERONET sky-scan particle property retrievals than AOD values. To effect comparisons with MISR, we accepted any case where at least two good-quality sky-scan results fall within a 4 h window centered on the MISR overpass time. If there are multiple, successful AERONET sky-scan retrievals within the window, SSA values are averaged. An assumption underlying this approach is that within an aerosol air mass, particle type varies less than AOD; there is some observational support for this assumption [e.g., Anderson *et al.*, 2003], though there are likely to be exceptions [e.g., Kahn *et al.*, 2007a], especially near sources or when multiple aerosol layers of different types are present. In practice, about 80% of the cases included have at least one measurement on each side of the overpass time; the rest have at least two measurements on one side of the overpass window.

[24] Table 4 summarizes the sampling statistics for the entire data set, stratified by season and expected aerosol type. Over 8 years we obtained 5156 coincident, central MISR-AERONET AOD observations that met the data selection criteria and 2130 central sky-scan results. There are over 1300 central AOD events for each of the Continental and Urban aerosol sites, over 650 each for Biomass Burning and Dusty, over 600 for Hybrid, and not quite 400 for the Maritime categories. There are about 650 sky-scan coincidences for Urban, just under 500 for Continental, about 300 each for Biomass Burning, Dusty, and Hybrid, and 81 for Maritime. Frequent cloud contamination and relatively few available sites contribute to lower sampling for Maritime sites.

[25] Also listed in Table 4 are the numbers of events in each category for which the lowest residual aerosol mixture in the MISR V22 product contained (a) only spherical, nonabsorbing particles, (b) both spherical absorbing and spherical nonabsorbing particles, or (c) both nonspherical mineral dust and spherical nonabsorbing particles. Although the lowest residual mixture is unique, more than one mixture



**Table 2.** MISR Version 22 Aerosol Component Optical Models<sup>a</sup>

No.	Component Name	$r_1$ ( $\mu\text{m}$ )	$r_2$ ( $\mu\text{m}$ )	$r_c$ ( $\mu\text{m}$ )	$\sigma$	SSA (446)	SSA (558)	SSA (672)	SSA (866)	AOD(446)/ AOD(558)	AOD(672)/ AOD(558)	AOD(867)/ AOD(558)	$g$ (558)	Particle Size/Shape Category
1	sph_nonabsorb_0.06	0.001	0.4	0.03	1.65	1.00	1.00	1.00	1.00	1.95	0.55	0.23	0.352	Small spherical
2	sph_nonabsorb_0.12	0.001	0.75	0.06	1.7	1.00	1.00	1.00	1.00	1.54	0.66	0.35	0.609	Small spherical
3	sph_nonabsorb_0.26	0.01	1.5	0.12	1.75	1.00	1.00	1.00	1.00	1.18	0.82	0.58	0.717	Medium spherical
6	sph_nonabsorb_2.80	0.10	50	1.0	1.9	1.00	1.00	1.00	1.00	0.99	1.02	1.06	0.776	Large spherical
8	sph_absorb_0.12_ssa_green_0.9	0.001	0.75	0.06	1.7	0.91	0.90	0.89	0.85	1.50	0.68	0.37	0.612	Small spherical, moderately absorbing
14	sph_absorb_0.12_ssa_green_0.8	0.001	0.75	0.06	1.7	0.82	0.80	0.77	0.72	1.47	0.69	0.40	0.614	Small spherical, strongly absorbing
19	Medium_grains	0.10	1.00	0.5	1.5	0.92	0.98	0.99	1.00	0.90	1.06	1.08	0.711	Medium dust
21	Coarse_spheroids	0.10	6.0	1.0	2.0	0.81	0.90	0.97	0.98	0.99	1.02	1.05	0.772	Coarse dust

<sup>a</sup>AOD, aerosol optical depth; SSA, single-scattering albedo. These aerosol optical models apply to the MISR standard level 2AS aerosol product, Versions 16 through 22. A number-weighted, log-normal particle size distribution function is adopted for all components. Aerosol components are named based on particle shape (spherical grains, nonspherical grains, or spheroids), SSA (nonabsorbing or absorbing), and effective radius ( $\mu\text{m}$ ). For absorbing aerosols the green-band SSA is also given. Single-scattering properties were calculated using a Mie code for spherical particles; dust component properties were calculated using the discrete dipole and  $T$ -matrix approaches for medium and coarse modes, respectively [Kalashnikova et al., 2005]. Wavelength (nm) is specified in parentheses where appropriate.  $r_1$  and  $r_2$  are the upper and lower limits of the size distribution;  $r_c$  and  $\sigma$  are the characteristic radius and width parameters in the log-normal distribution. The asymmetry parameter ( $g$ ) will generally represent particle scattering phase functions poorly for the purpose of calculating MISR multiangle radiances and is given here only in the MISR green band for reference; full phase functions are available in the MISR standard product "ACP\_APOP" files. All spherical components are assumed to be distributed vertically within 10 km of the surface and have scale heights of 2 km. Medium and coarse dust are confined to the lowest 10 km.

can meet the chi-square criteria for a successful retrieval. These data are discussed in the next section.

### 3. MISR Aerosol Optical Depth (AOD) Retrieval Assessment

[26] Figure 2 and Table 5 report the overall group average MISR-AERONET midvisible (558 nm) AOD difference statistics by probable aerosol category, as well as summary statistics derived in paper 1 based on similar aerosol-type groupings for the V12 algorithm. Table 5 also contains the corresponding site-specific data. Figure 2 compares the AERONET values with the MISR central and surrounding retrieval regions for each category. Of 5156 coincidences, 125 significant outliers (2.4%), where the MISR AOD is more than 2.5 times higher than the AERONET AOD, and 68 (1.3%) where the MISR AOD is less than 60% of the corresponding AERONET value, have been removed from the statistics in Table 5 and Figure 2. Of the high outliers, 61% are attributable to spatial and/or temporal scene variability, convolved with the differences between MISR and AERONET sampling, rather than retrieval error. This conclusion is based on variability in the retrieval results from the central vs. surrounding regions and/or the AERONET time series. About an additional 35% of the high outliers are likely due to variability as well, including cases having nearby scattered or broken cloud. The corresponding values for the low AOD outliers are 63% and 22%, respectively. Sampling outliers can occur if an aerosol plume is found in the MISR image but misses the AERONET field of view (FOV) or if a plume fills the AERONET FOV but accounts for only a small fraction of the MISR retrieval region. So for both the high and the low outliers of significant magnitude, more than 80% are likely due to sampling differences. A similar result was obtained in paper 1. About 15% of the 68 MISR low outliers in this data set are cases where MISR adopted an unduly high particle SSA compared to AERONET. Other factors, including algorithmic issues, account for the remaining cases; these issues are explored in more detail.

[27] In Figure 2, focus first on the position along the horizontal axis of the filled diamond and circle symbols, connected with solid lines. These represent the category-specific percentage of cases for which the MISR central AOD is within 0.05 or 20%  $\times$  AOD, and 0.03 or 10%  $\times$  AOD, of the near-coincident AERONET value, respectively. The results vary considerably, depending on category. For V22, about 70% to 75% fall within 0.05 or 20%  $\times$  AOD of the validation data, and about 50% to 55% meet the 0.03 or 10%  $\times$  AOD criterion, except in the Dusty and Hybrid (smoke + dust) categories. The open diamond and circle symbols and dashed lines plot the corresponding values for the V12 algorithm. For the 0.05 or 20%  $\times$  AOD criterion, the V22 values are about 10%, 7%, and 6% higher than those for V12 for the Biomass Burning, Continental, and Maritime aerosol categories, respectively, reflecting improvements made to the retrieval algorithm as mentioned in section 1. For the Dusty category the agreement is about 5% poorer, owing in part to a lack of medium-mode spherical particles in the V22 component set (section 4.2); the other categories were not independently tracked in the earlier, smaller data set, though the need to add mixtures of dust and smoke optical analogs to the algorithm for what we designate



**Table 3.** MISR Version 22 Aerosol Mixture Properties<sup>a</sup>

Mixture No.	Component Fractional AOD (at 558 nm)								AOD Relative to Green			Single-Scattering Albedo				ANG
	1	2	3	6	8	14	19	21	Blue	Red	NIR	Blue	Green	Red	NIR	
Spherical, Nonabsorbing Mixtures																
1	1	-	-	-	-	-	-	-	1.95	0.549	0.23	1	1	1	1	3.23
2	0.95	-	-	0.05	-	-	-	-	1.9	0.573	0.271	1	1	1	1	2.94
3	0.9	-	-	0.1	-	-	-	-	1.85	0.596	0.312	1	1	1	1	2.69
4	0.8	-	-	0.2	-	-	-	-	1.76	0.644	0.395	1	1	1	1	2.26
5	0.7	-	-	0.3	-	-	-	-	1.66	0.691	0.477	1	1	1	1	1.88
6	0.6	-	-	0.4	-	-	-	-	1.57	0.738	0.559	1	1	1	1	1.55
7	0.5	-	-	0.5	-	-	-	-	1.47	0.786	0.642	1	1	1	1	1.24
8	0.4	-	-	0.6	-	-	-	-	1.37	0.833	0.724	1	1	1	1	0.96
9	0.3	-	-	0.7	-	-	-	-	1.28	0.881	0.807	1	1	1	1	0.69
10	0.2	-	-	0.8	-	-	-	-	1.18	0.928	0.889	1	1	1	1	0.42
11	-	1	-	-	-	-	-	-	1.54	0.66	0.348	1	1	1	1	2.24
12	-	0.95	-	0.05	-	-	-	-	1.51	0.679	0.384	1	1	1	1	2.07
13	-	0.9	-	0.1	-	-	-	-	1.49	0.697	0.419	1	1	1	1	1.91
14	-	0.8	-	0.2	-	-	-	-	1.43	0.733	0.49	1	1	1	1	1.62
15	-	0.7	-	0.3	-	-	-	-	1.38	0.769	0.56	1	1	1	1	1.36
16	-	0.6	-	0.4	-	-	-	-	1.32	0.805	0.631	1	1	1	1	1.11
17	-	0.5	-	0.5	-	-	-	-	1.26	0.842	0.701	1	1	1	1	0.89
18	-	0.4	-	0.6	-	-	-	-	1.21	0.878	0.772	1	1	1	1	0.68
19	-	0.3	-	0.7	-	-	-	-	1.15	0.914	0.843	1	1	1	1	0.47
20	-	0.2	-	0.8	-	-	-	-	1.1	0.95	0.913	1	1	1	1	0.28
21	-	-	1	-	-	-	-	-	1.18	0.82	0.576	1	1	1	1	1.09
22	-	-	0.95	0.05	-	-	-	-	1.17	0.83	0.6	1	1	1	1	1.02
23	-	-	0.9	0.1	-	-	-	-	1.17	0.841	0.624	1	1	1	1	0.94
24	-	-	0.8	0.2	-	-	-	-	1.15	0.861	0.672	1	1	1	1	0.81
25	-	-	0.7	0.3	-	-	-	-	1.13	0.881	0.72	1	1	1	1	0.68
26	-	-	0.6	0.4	-	-	-	-	1.11	0.901	0.767	1	1	1	1	0.55
27	-	-	0.5	0.5	-	-	-	-	1.09	0.921	0.815	1	1	1	1	0.43
28	-	-	0.4	0.6	-	-	-	-	1.07	0.942	0.863	1	1	1	1	0.32
29	-	-	0.3	0.7	-	-	-	-	1.05	0.962	0.911	1	1	1	1	0.21
30	-	-	0.2	0.8	-	-	-	-	1.03	0.982	0.959	1	1	1	1	0.10
Spherical, Absorbing + Nonabsorbing Mixtures																
31	-	-	-	-	1	-	-	-	1.51	0.677	0.375	0.911	0.9	0.885	0.8	2.10
32	-	-	-	0.05	0.95	-	-	-	1.48	0.694	0.409	0.914	0.905	0.894	0.8	1.96
33	-	-	-	0.1	0.9	-	-	-	1.45	0.712	0.443	0.917	0.91	0.902	0.8	1.80
34	-	-	-	0.2	0.8	-	-	-	1.4	0.746	0.511	0.924	0.92	0.917	0.9	1.53
35	-	-	-	0.3	0.7	-	-	-	1.35	0.781	0.578	0.931	0.93	0.93	0.9	1.28
36	-	-	-	0.4	0.6	-	-	-	1.3	0.815	0.646	0.938	0.94	0.943	0.9	1.05
37	-	-	-	0.5	0.5	-	-	-	1.25	0.85	0.714	0.946	0.95	0.954	0.9	0.84
38	-	-	-	0.6	0.4	-	-	-	1.2	0.884	0.782	0.955	0.96	0.965	0.9	0.64
39	-	-	-	0.7	0.3	-	-	-	1.14	0.919	0.85	0.965	0.97	0.975	0.9	0.44
40	-	-	-	0.8	0.2	-	-	-	1.09	0.953	0.918	0.976	0.98	0.984	0.9	0.26
41	-	-	-	-	-	1	-	-	1.47	0.695	0.403	0.821	0.8	0.773	0.7	1.95
42	-	-	-	0.05	-	0.95	-	-	1.45	0.712	0.436	0.827	0.81	0.79	0.7	1.81
43	-	-	-	0.1	-	0.9	-	-	1.42	0.728	0.468	0.833	0.82	0.805	0.7	1.68
44	-	-	-	0.2	-	0.8	-	-	1.37	0.761	0.533	0.847	0.84	0.834	0.8	1.43
45	-	-	-	0.3	-	0.7	-	-	1.33	0.793	0.598	0.861	0.86	0.861	0.8	1.20
46	-	-	-	0.4	-	0.6	-	-	1.28	0.826	0.664	0.876	0.88	0.886	0.8	0.99
47	-	-	-	0.5	-	0.5	-	-	1.23	0.859	0.729	0.893	0.9	0.908	0.9	0.79
48	-	-	-	0.6	-	0.4	-	-	1.18	0.892	0.794	0.911	0.92	0.929	0.9	0.60
49	-	-	-	0.7	-	0.3	-	-	1.13	0.924	0.859	0.93	0.94	0.949	0.9	0.42
50	-	-	-	0.8	-	0.2	-	-	1.08	0.957	0.924	0.952	0.96	0.967	0.9	0.24
Dust Mixtures																
51	-	0.72	-	0.08	-	-	0.2	-	1.37	0.77	0.551	0.989	0.995	0.998	0.9	1.37
52	-	0.48	-	0.32	-	-	0.2	-	1.24	0.857	0.72	0.988	0.995	0.999	0.9	0.81
53	-	0.16	-	0.64	-	-	0.2	-	1.06	0.973	0.946	0.986	0.995	0.999	0.9	0.17
54	-	0.54	-	0.06	-	-	0.4	-	1.25	0.844	0.683	0.977	0.991	0.997	0.9	0.91
55	-	0.36	-	0.24	-	-	0.4	-	1.15	0.909	0.81	0.975	0.991	0.997	0.9	0.53
56	-	0.12	-	0.48	-	-	0.4	-	1.02	0.996	0.979	0.972	0.991	0.998	0.9	0.05
57	-	0.36	-	0.04	-	-	0.6	-	1.13	0.918	0.815	0.962	0.986	0.996	0.9	0.49
58	-	0.24	-	0.16	-	-	0.6	-	1.07	0.961	0.9	0.959	0.986	0.996	0.9	0.25
59	-	0.08	-	0.32	-	-	0.6	-	0.977	1.02	1.01	0.956	0.986	0.997	0.9	-0.06
60	-	0.18	-	0.02	-	-	0.8	-	1.01	0.991	0.947	0.943	0.982	0.995	0.9	0.10
61	-	0.12	-	0.08	-	-	0.8	-	0.98	1.01	0.989	0.941	0.982	0.995	0.9	-0.02
62	-	0.04	-	0.16	-	-	0.8	-	0.936	1.04	1.05	0.938	0.982	0.995	0.9	-0.17
63	-	0.4	-	-	-	-	0.48	0.12	1.16	0.898	0.783	0.951	0.977	0.993	0.9	0.60
64	-	0.4	-	-	-	-	0.36	0.24	1.18	0.892	0.78	0.94	0.968	0.99	0.9	0.62
65	-	0.4	-	-	-	-	0.24	0.36	1.19	0.887	0.776	0.928	0.959	0.986	0.9	0.64

**Table 3.** (continued)

Mixture No.	Component Fractional AOD (at 558 nm)								AOD Relative to Green			Single-Scattering Albedo				ANG
	1	2	3	6	8	14	19	21	Blue	Red	NIR	Blue	Green	Red	NIR	
66	-	0.4	-	-	-	-	0.12	0.48	1.2	0.881	0.773	0.918	0.95	0.983	0.9	0.66
67	-	0.2	-	-	-	-	0.64	0.16	1.04	0.977	0.928	0.927	0.97	0.991	0.9	0.17
68	-	0.2	-	-	-	-	0.48	0.32	1.05	0.969	0.924	0.91	0.958	0.987	0.9	0.20
69	-	0.2	-	-	-	-	0.32	0.48	1.07	0.962	0.919	0.894	0.946	0.983	0.9	0.23
70	-	0.2	-	-	-	-	0.16	0.64	1.08	0.954	0.914	0.879	0.934	0.979	0.9	0.25
71	-	-	-	-	-	-	0.8	0.2	0.914	1.06	1.07	0.896	0.962	0.99	0.9	-0.24
72	-	-	-	-	-	-	0.6	0.4	0.933	1.05	1.07	0.873	0.947	0.985	0.9	-0.20
73	-	-	-	-	-	-	0.4	0.6	0.951	1.04	1.06	0.851	0.932	0.98	0.9	-0.17
74	-	-	-	-	-	-	0.2	0.8	0.97	1.03	1.06	0.83	0.917	0.976	0.9	-0.13

<sup>a</sup>ANG, Angstrom exponent; AOD, aerosol optical depth. The eight components used in this mixture table are described in Table 2.

here as the Hybrid category (discussed in section 3.3), was also raised in paper 1. Similar relationships among the categories, and between the V12 and the V22 results, are found for the more stringent 0.03 or 10%  $\times$  AOD criterion.

[28] Placement along the vertical axis in Figure 2 compares the AERONET 2 h averaged values with the spatial average of MISR AOD results for the central and as many of the eight surrounding regions as have successful retrievals, as well as with those for the central region alone. The difference plotted accounts to some degree for variability; for points above the zero line the larger-spatial-scale ( $\sim 50$  km) central + surrounding region average produces systematically better agreement with AERONET than the single-region (17.6 km) central comparison. For points below the zero line it is advantageous for the MISR retrieval regions to be collocated with the AERONET site as closely as possible. These results by category are statistically fairly robust, as each large symbol represents hundreds to more than 1000 MISR-AERONET comparisons, though the sampling varies significantly for individual sites (Table 5).

[29] Focusing again on the filled symbols in Figure 2, the larger-scale averaging produces 2% to 3% better agreement for the Continental and Biomass Burning categories, 5% better agreement for Dusty, and almost 8% for the Maritime category, whereas the central region provides better agreement for the Urban class and marginally better agreement for the less-well-sampled Hybrid class. In Urban regions, where AOD variability is expected to be dominant on short spatial scales, the central regions have a systematic advantage in representing the AERONET 2 h window measurements [Jiang *et al.*, 2007]. Site-specific values illustrate this point. For example, Mexico City is responsible for an Urban outlier that would plot along the vertical axis in Figure 2 at about -32% (Table 5). By contrast, for Maritime situations, where aerosols are generally more uniform on 10 to 100 km scales, the larger spatial averaging reduces the impact of serendipitous aerosol air mass edges and AOD gradients sampled differently by the satellite and surface stations [Kahn *et al.*, 2007a, sec. 3.2]. Similarly, at Continental sites such as El Arenosillo in southern Spain and Arica in northern Chile, regional averaging produces significantly better agreement with the AERONET time series. Site-to-site differences in regional source characteristics, topography, and meteorology account for the scatter among AERONET stations within each category, but overall, the variability patterns are distinct and are consistent with expectations.

[30] Figure 3 looks in more detail at the MISR-AERONET midvisible AOD comparisons, showing both scatter and difference plots, stratified by season and by the six expected aerosol air-mass-type groupings already described. The middle row in Figure 3 focuses on the low-AOD range of the scatterplots in the top row and uses open circles to improve the visibility of individual events.

[31] The data exhibit many expected patterns, such as a Maritime AOD generally below 0.3 and high-AOD events, in excess of 0.6, occurring preferentially for the Biomass Burning, Dusty, Urban, and Hybrid categories. The quantitative ranges of values are somewhat higher than the corresponding ones in paper 1, owing to the much greater sampling in the current data collection, which captures a broader spectrum of naturally occurring conditions. Although these MISR validation data subsets were chosen for coincidence with AERONET rather than being optimized to represent the “global-average” AOD, they cover a diversity of situations. As such, they illustrate one reason for obtaining longer-term, climate-quality data records; as larger data sets are acquired, it will become possible to separate with greater confidence sampling effects from natural patterns, trends, and extreme events, and an increasingly robust environmental picture will emerge. This is true for the validation process itself as well. Having provided an overview based on Figures 2 and 3, we now explore individual strata in more detail.

### 3.1. AOD Performance at Very Low AOD and Maritime Sites

[32] When the AOD is very low, MISR tends to overestimate the AOD for a small but significant fraction of cases in all aerosol types. The concentrations of points above the zero lines in the difference plots along the bottom row in Figure 3, when the AOD is low, illustrate this condition. The middle row of plots in Figure 3 reveals a gap of about +0.025 in the MISR midvisible AOD values near 0. This gap does not appear in the AERONET validation data, as is especially clear for the well-sampled Biomass Burning and Continental category plots. Comparison between MISR and a much larger number of coincident MODIS/Terra observations shows similar MISR behavior [Kahn *et al.*, 2009a, Figure 5].

[33] Previous work removed about half of an  $\sim 0.05$  high bias, evident in the early postlaunch (V12) MISR AOD over-ocean product, when the MISR band-to-band and camera-to-camera calibrations were corrected [Diner *et al.*, 2004; Kahn *et al.*, 2005b; Bruegge *et al.*, 2007]. These

**Table 4.** Aerosol Optical Depth (AOD) and Sky-Scan Coincidence Sampling, by Season and Aerosol Type<sup>a</sup>

	Total	DJF	MAM	JJA	SON
<b>Biomass Burning</b>					
Central AOD	662	91	159	248	164
Surrounding AOD	653	89	157	244	163
Central sky scan	318	39	75	110	94
Lowest residual					
Nonabsorbing	383	57	99	139	88
Absorbing	199	17	43	90	49
Dusty	80	17	17	19	27
<b>Continental</b>					
Central AOD	1348	202	326	488	332
Surrounding AOD	1342	200	325	486	331
Central sky scan	496	90	134	130	130
Lowest residual					
Nonabsorbing	990	158	218	357	257
Absorbing	178	22	44	71	41
Dusty	180	22	64	60	34
<b>Dusty</b>					
Central AOD	645	118	161	196	170
Surrounding AOD	641	117	159	196	169
Central sky scan	300	41	81	101	77
Lowest residual					
Nonabsorbing	299	67	63	72	97
Absorbing	120	30	26	22	42
Dusty	226	21	72	102	31
<b>Maritime</b>					
Central AOD	378	90	100	99	89
Surrounding AOD	378	90	100	99	89
Central sky scan	81	20	27	19	15
Lowest residual					
Nonabsorbing	157	41	36	48	32
Absorbing	61	11	10	23	17
Dusty	160	38	54	43	59
<b>Urban</b>					
Central AOD	1498	255	424	366	453
Surrounding AOD	1480	249	420	363	448
Central sky scan	648	122	180	103	243
Lowest residual					
Nonabsorbing	1027	170	269	275	313
Absorbing	242	49	64	48	81
Dusty	229	36	91	43	59
<b>Hybrid BD</b>					
Central AOD	625	188	155	110	172
Surrounding AOD	620	187	153	109	171
Central sky scan	287	98	70	36	83
Lowest residual					
Nonabsorbing	227	63	33	42	89
Absorbing	131	33	32	29	37
Dusty	267	92	90	39	46

<sup>a</sup>Nonabsorbing mixtures are Nos. 1–30, absorbing mixtures are Nos. 31–50, and dusty mixtures are Nos. 51–74 in Table 3.

corrections were identified from direct radiometric tests, independent of aerosol-retrieval-related considerations. The ~6% improvement in MISR-AERONET AOD agreement at Maritime sites between V12 and V22 (Figure 2) is traced primarily to these calibration corrections. The gap that appears in the row 2 plots in Figure 3 is comparable in magnitude to the remaining high MISR AOD bias relative to AERONET that shows up at low AODs in the row 3 difference plots in Figure 3, and could account statistically for much or all of it.

[34] There are relatively few coincident, over-water MISR-AERONET retrievals in our data set, owing to the small number of AERONET island sites, frequent cloud cover over open ocean, and silt or pollution in surface waters along many coasts that makes them unsuitable for dark-water retrievals. However, over ocean, scene conditions are typically more uniform than over land, so it is easier to identify small artifacts in the retrieved values. In the much larger coincident MISR-MODIS over-ocean data set used by Kahn *et al.* [2009a, Figure 5], MISR V22 AOD values, especially below about 0.25, show AOD quantization noise in approximately 0.025 increments, in addition to the gap near 0 AOD. These low-AOD features are artifacts of the MISR V22 retrieval algorithm, which interpolates AOD values from a grid with 0.025 spacing.

[35] Near coasts, where at times pollution, runoff, or ocean biological activity can significantly increase surface water reflectivity, MISR AOD can be skewed high, because the MISR over-water algorithm assumes that the ocean surface is dark in the red and near-infrared spectral bands used [e.g., Kahn *et al.*, 2007a, their section 3.1]. Figure 4 takes a closer look at MISR-AERONET coincidences over water, focusing exclusively on retrievals done with the MISR over-water algorithm and including AOD observations coincident with the AERONET MAN [Smirnov *et al.*, 2009] as well as island stations. The vast majority of the 282 island plus 61 MAN cases show very low AOD. They fall within 0.05 of the red center line, offset by +0.025, as expected based on the earlier analysis, and scatter uniformly about this line.

[36] The outliers in Figure 4 include 12 scenes dominated by broken cloud or dust plumes, identified based on visual inspection of the image data, and marked with plus symbols; in these cases, cloud contamination or scene variability are likely factors contributing to the observed discrepancies. Data from two AERONET stations in the shallow, polluted waters of the Arabian Gulf not included in the general MISR-AERONET coincidence data set in this paper (Table 1) are highlighted with orange exes. For this population of 63 points, MISR values tend to be skewed high relative to AERONET values, as well as to the +0.025 line. Most cases unaffected by surface pollution or scene variability, for which the AERONET AOD is greater than about 0.5, fall below the zero difference line, as also observed for the over-land categories, but sampling is too poor to draw strong conclusions. MISR AOD behavior in coastal regions is discussed further in section 3.4.

### 3.2. AOD Performance at Biomass Burning Sites

[37] Focusing specifically on the Biomass Burning category, the MISR mean AOD is well within the envelopes already described, with 76% of cases falling within 0.05 or 20%  $\times$  AOD of the near-coincident AERONET values, and 55% within 0.03 or 10%  $\times$  AOD (Figure 2 and Table 5). These statistics cover all months of the year, whereas for most Biomass Burning sites, actual burning occurs only during a specific season, so the plots include both periods when small to medium, spherical, smoke particles dominate the aerosol load and times when background particles prevail.

[38] Seasonal information is given by the colors in Figure 3; summer and autumn burning-season events occurring in

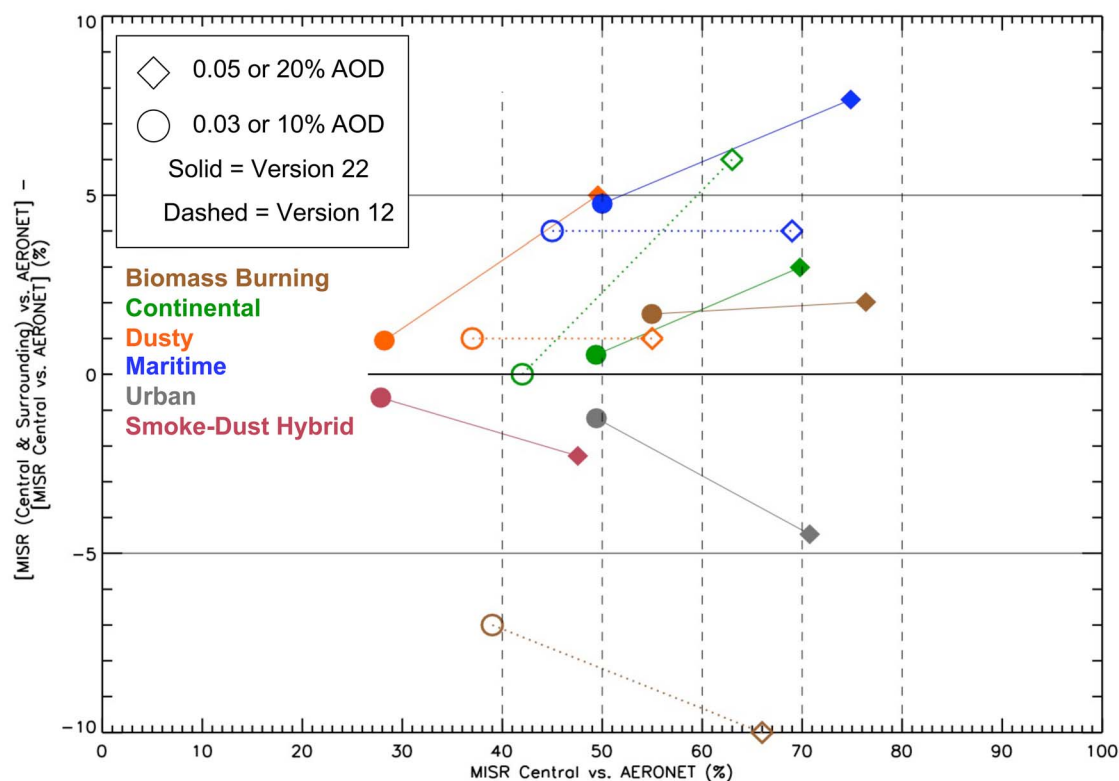


**Figure 2.** Multiangle Imaging SpectroRadiometer (MISR)–Aerosol Robotic Network (AERONET) mean aerosol optical depth (AOD) difference (%) for 5156 coincidences, stratified according to the aerosol air-mass type class that frequently dominates the site. Comparisons between MISR central retrieval region AODs and near-coincident AERONET values are shown along the horizontal axis. The vertical axis gives the difference between the MISR AOD, assessed as the average of the central plus all available of the eight surrounding regions, and the corresponding value assessed using the MISR central region only. Filled diamonds represent the class-average percentage meeting the  $[0.05 \text{ or } 20\% \times \text{AOD}]$  criterion. Filled circles plot the class-average percentage meeting the more stringent  $[0.03 \text{ or } 10\% \times \text{AOD}]$  criterion. Open symbols show corresponding class-average results for the MISR Version 12 (V12) product from Kahn *et al.* [2005a]. Colors are used to distinguish aerosol type classes, as indicated in the legend. Lines connect the symbols for clarity. Numerical values for the central retrieval region statistics, along with the number of counts per site and per class, as well as site-specific statistics, are listed in Table 5. One hundred ninety-three outliers were removed from the MISR central statistics but not from the central + surroundings statistics.

much of the Northern Hemisphere appear in green and orange, respectively. Where deviations occur, especially for AODs  $> 0.2$ , the MISR value tends to be skewed low relative to the AERONET value (lower left plot in Figure 3). The same pattern was observed at biomass burning sites in paper 1, as well as for specific biomass burning events by Chen *et al.* [2008] and for pollution aerosols in East Asia and at the eastern end of the Indo-Gangetic plain [Kahn *et al.*, 2009a, Figure 6]. The AOD underestimation was traced in those studies to a lack of mixtures containing spherical particles having sufficiently low SSA in the MISR standard algorithm. This interpretation is supported by comparisons between MISR- and AERONET-retrieved SSA discussed in section 4.3; if the aerosol SSA adopted by the MISR algorithm is too high, fewer particles are required to produce the scattered-light signal observed, and the retrieved AOD will be skewed low. In nearly two thirds of the 68 outliers where the MISR AOD is less than 60% of the

AERONET value, dark particles, either biomass burning or urban pollution, are expected. For a few of these events, for example, at Arica, Yulin, and Ispra, the AERONET-retrieved SSA is both reliable (i.e., the AERONET 440 nm AOD  $> 0.4$ ) and substantially lower than the SSA obtained from the corresponding MISR retrieval. And for many others the scene is hazy and the surrounding MISR retrieval regions produce higher AODs, conditions typical of smoke and urban pollution plumes.

[39] As noted in the previously cited publications, the MISR V22 algorithm climatology includes only one size of spherical particles having an SSA other than unity (Table 2), and the algorithm is forced to select among the available choices for particle size and/or SSA. However, there are events where the MISR-retrieved AOD is substantially lower than the corresponding AERONET value and the actual particle SSA is at or very near unity, especially for non-biomass burning cases where AOD  $\gtrsim 0.5$  (Figure 3,

**Table 5.** MISR-AERONET Green-Band AOD Comparison Statistics for Central Regions Without Outliers and for Surroundings, Stratified by Site and by Expected Aerosol Type Category<sup>a</sup>

Site	Count	MISR AOD			AERONET AOD			Mean Absolute Diff. (Rel. %)	AOD Gain	AOD Offset	AOD: 20%, or 0.05	AOD: 10%, or 0.03	DAOD: Surr. – Central <sup>b</sup>	VI2 AOD: 20%, or 0.05/10%, or 0.03 <sup>b</sup>
		Mean	SD		Mean	SD								
<b>Biomass Burning</b>	<b>635</b>	<b>0.191</b>	<b>0.024</b>		<b>0.215</b>	<b>0.013</b>			<b>0.653</b>	<b>0.050</b>	<b>76.38</b>	<b>54.96</b>	<b>2.0/1.7</b>	<b>66/39</b>
Abracos_Hill	31	0.242	0.018		0.300	0.017		32.49	0.700	0.032	74.19	54.84	0.8/–1.7	
Mukdahan	54	0.332	0.027		0.396	0.022		19.97	0.740	0.039	62.96	46.30	–5.6/–9.3	
Mongu	165	0.213	0.025		0.217	0.011		22.39	0.837	0.031	87.27	69.09	2.5/3.8	
Skukuza	123	0.141	0.019		0.154	0.008		23.81	0.834	0.013	86.99	66.67	2.5/1.1	
Jabiru	85	0.103	0.023		0.109	0.009		26.99	0.838	0.011	87.06	67.06	3.6/7.4	
Rio Branco	16	0.321	0.031		0.501	0.024		30.66	0.470	0.085	37.50	25.00	12.5/–6.3	
Alta Floresta	32	0.310	0.028		0.443	0.036		31.31	0.530	0.075	59.38	37.50	10.3/1.9	
Cuiaba-Miranda	33	0.246	0.028		0.349	0.024		31.96	0.688	0.006	57.58	18.18	–6.2/8.8	
Santa Cruz	19	0.158	0.025		0.161	0.011		36.11	0.481	0.081	68.42	42.11	21.1/10.5	
Bonanza Creek	26	0.071	0.007		0.057	0.005		55.77	0.802	0.025	80.77	65.39	3.8/7.7	
Tinga_Tingana	51	0.130	0.033		0.074	0.008		104.67	1.064	0.050	49.02	13.73	4.6/6.6	
<b>Dusty</b>	<b>585</b>	<b>0.283</b>	<b>0.039</b>		<b>0.270</b>	<b>0.015</b>		<b>50.83</b>	<b>0.766</b>	<b>0.077</b>	<b>49.57</b>	<b>28.21</b>	<b>5.0/0.9</b>	<b>55/37</b>
Mezaira	12	0.392	0.077		0.352	0.011		21.11	0.901	0.075	83.33	50.00	0.0/16.7	
Capo Verde	71	0.356	0.032		0.367	0.018		22.30	0.872	0.037	54.93	29.58	7.0/1.55	
Dhaddah	37	0.377	0.049		0.404	0.020		23.37	0.946	–0.005	43.24	35.14	9.4/–6.2	
Solar_Village	108	0.378	0.062		0.341	0.019		26.03	0.735	0.127	58.33	37.04	–1.1/–8.9	
Amnyon	19	0.389	0.026		0.524	0.035		26.39	0.723	0.010	36.84	26.32	–11.8/–11.3	
Mussafa	30	0.343	0.046		0.303	0.018		29.55	1.072	0.018	50.00	33.33	30.0/13.3	
Dakar	70	0.332	0.034		0.440	0.020		30.11	0.719	0.016	32.86	14.29	10.8/2.6	
Hamim	39	0.380	0.056		0.286	0.014		37.49	1.291	0.011	33.33	23.08	–5.1/–7.7	
Dalanzadgad	86	0.139	0.018		0.090	0.009		78.64	0.928	0.055	59.30	31.40	–5.1/–0.6	
Railroad_Valley	99	0.117	0.025		0.064	0.005		107.56	1.143	0.044	50.51	24.24	17.3/6.3	
Brdsville	14	0.123	0.035		0.057	0.005		132.49	1.421	0.041	21.43	0.00	–6.0/3.8	
<b>Continental</b>	<b>1294</b>	<b>0.142</b>	<b>0.030</b>		<b>0.128</b>	<b>0.010</b>		<b>49.00</b>	<b>0.721</b>	<b>0.050</b>	<b>69.78</b>	<b>49.38</b>	<b>3.0/0.5</b>	<b>63/42</b>
Pimai	43	0.314	0.035		0.357	0.022		20.07	0.615	0.095	62.79	41.86	18.6/11.6	
Nes_Ziona	75	0.230	0.047		0.273	0.023		21.56	0.799	0.012	64.00	34.67	8.0/13.3	
Toravere	40	0.124	0.012		0.123	0.009		22.05	0.917	0.011	92.50	77.50	–2.0/5.8	
Arica	43	0.201	0.039		0.264	0.016		29.91	0.698	0.017	44.19	23.26	26.9/19.0	
El_Arenosillo	36	0.160	0.033		0.208	0.011		30.51	0.714	0.012	44.44	27.78	37.6/26.1	
Konza_EDC	106	0.114	0.021		0.109	0.008		30.84	0.686	0.039	86.79	72.64	2.9/4.9	
Cordoba-CETT	93	0.064	0.012		0.075	0.008		32.28	0.621	0.017	93.55	82.80	0.1/0.4	
Cart_Site	76	0.125	0.026		0.105	0.007		36.69	0.874	0.033	84.21	64.47	2.8/–2.1	
Bondville	76	0.123	0.021		0.123	0.009		38.00	0.635	0.045	82.90	59.21	–3.9/–10.5	
Forth_Crete	8	0.202	0.018		0.314	0.014		38.59	1.234	–0.186	37.50	0.00	18.1/11.1	
Sioux_Falls	69	0.112	0.018		0.096	0.007		39.47	1.059	0.010	81.16	68.12	1.7/–1.0	
Rimrock	72	0.106	0.021		0.081	0.006		50.94	0.999	0.025	77.78	50.00	16.9/26.0	
Boulder	105	0.121	0.034		0.092	0.008		53.23	0.906	0.038	72.38	57.14	–2.0/–7.1	
COVE	74	0.213	0.028		0.175	0.016		53.45	0.934	0.049	68.92	33.78	–4.1/0.0	
Martcopa	99	0.128	0.038		0.091	0.007		55.72	0.940	0.043	68.69	48.49	2.3/–4.5	
Bratts_Lake	64	0.127	0.023		0.107	0.011		56.31	0.507	0.073	78.13	59.38	–3.9/–9.4	
Sevilleta	70	0.159	0.049		0.095	0.006		90.88	1.004	0.064	32.86	20.00	4.6/2.5	
Rogers_Dry_Lake	145	0.135	0.045		0.074	0.005		96.43	1.343	0.036	46.21	19.31	–4.3/–11.5	

Table 5. (continued)

Site	Count	MISR AOD		AERONET AOD		AOD Corr.	Mean Absolute Diff. (Rel. %)	AOD Gain	AOD Offset	AOD: 20%, or 0.05	AOD: 10%, or 0.03	DAOD: Surr. – Central <sup>b</sup>	V12 AOD: 20%, or 0.05/10%, or 0.03 <sup>b</sup>
		Mean	SD	Mean	SD								
<b>Urban</b>	<b>1467</b>	<b>0.203</b>	<b>0.028</b>	<b>0.237</b>	<b>0.021</b>	<b>0.924</b>	<b>26.90</b>	<b>0.662</b>	<b>0.046</b>	<b>70.76</b>	<b>49.42</b>	<b>–4.5/–1.2</b>	
Belsk	23	0.182	0.020	0.197	0.020	0.964	14.22	0.938	–0.003	82.61	60.87	9.1/10.0	
Moscow	47	0.166	0.016	0.181	0.017	0.907	18.90	0.746	0.032	87.23	57.45	–4.3/10.6	
Mexico_City	56	0.243	0.031	0.273	0.043	0.918	20.02	0.748	0.039	71.43	44.64	–32.1/–21.4	
Bac_Giang	18	0.545	0.045	0.655	0.030	0.803	21.03	0.488	0.225	61.11	33.33	–16.7/–11.1	
Tomsk	31	0.168	0.021	0.196	0.017	0.973	21.16	0.779	0.016	80.65	61.29	–2.5/7.5	
MD_Science_Center	89	0.140	0.017	0.150	0.016	0.957	22.51	0.773	0.023	87.64	70.79	1.2/5.9	
Hamburg	60	0.159	0.017	0.160	0.017	0.921	22.81	0.961	0.005	85.00	65.00	0.0/3.3	
Shirahama	13	0.286	0.024	0.372	0.020	0.933	22.91	0.716	0.020	46.15	23.08	7.7/23.1	
Rome_Tor_Vergata	141	0.144	0.025	0.165	0.017	0.869	23.05	0.795	0.012	74.47	53.19	–7.6/–10.9	
Lille	39	0.155	0.021	0.186	0.017	0.935	23.77	0.736	0.018	71.80	51.28	5.1/5.1	
Beijing	113	0.292	0.041	0.381	0.033	0.930	24.21	0.620	0.056	54.87	38.94	1.7/–4.2	
Sao_Paulo	66	0.171	0.021	0.204	0.022	0.888	25.36	0.554	0.059	66.67	40.91	–2.0/3.2	
XiangHe	86	0.311	0.038	0.399	0.038	0.913	25.78	0.594	0.074	59.30	39.54	–1.8/1.8	
Kanpur	96	0.430	0.046	0.574	0.033	0.820	26.08	0.620	0.074	39.58	13.54	–6.6/1.9	
Thessaloniki	29	0.188	0.027	0.251	0.020	0.927	26.38	0.783	–0.008	48.28	31.03	–1.4/9.6	
Osaka	21	0.284	0.035	0.297	0.030	0.900	29.07	0.651	0.090	47.62	23.81	9.5/14.3	
Yulin	24	0.288	0.058	0.318	0.030	0.739	29.80	0.498	0.130	54.17	33.33	1.8/–1.3	
GSFC	116	0.109	0.012	0.111	0.009	0.948	30.99	0.678	0.034	93.10	82.76	2.6/–1.7	
Avignon	182	0.149	0.026	0.145	0.014	0.843	32.83	0.729	0.044	77.47	54.95	–3.6/–2.8	
Ispra	31	0.178	0.023	0.256	0.024	0.869	33.46	0.689	0.002	41.94	12.90	–1.9/13.8	
Fresno	116	0.146	0.040	0.138	0.010	0.746	33.85	0.597	0.063	78.45	52.59	–21.2/–13.3	
Minsk	19	0.175	0.018	0.167	0.013	0.930	35.46	1.064	–0.002	68.42	52.63	10.5/–5.3	
CCNY	51	0.168	0.025	0.184	0.014	0.914	35.62	0.727	0.034	70.59	45.10	–2.0/11.8	
<b>Maritime</b>	<b>366</b>	<b>0.117</b>	<b>0.018</b>	<b>0.095</b>	<b>0.008</b>	<b>0.870</b>	<b>53.69</b>	<b>0.801</b>	<b>0.041</b>	<b>74.86</b>	<b>50.00</b>	<b>7.7/4.8</b>	<b>69/45</b>
Ascension_Island	43	0.193	0.035	0.195	0.010	0.944	28.27	0.768	0.043	76.74	48.84	0.0/0.0	
Nauru	19	0.087	0.008	0.070	0.007	0.776	31.86	0.976	0.018	89.47	68.42	0.0/10.5	
Bermuda	10	0.123	0.016	0.116	0.008	0.572	39.66	0.320	0.086	60.00	60.00	30.0/0.0	
Midway_Island	50	0.108	0.013	0.079	0.007	0.935	40.86	1.160	0.016	88.00	60.00	6.0/8.0	
Tahiti	25	0.071	0.014	0.067	0.010	0.518	42.93	0.456	0.041	92.00	72.00	0.0/4.0	
Azores	9	0.100	0.016	0.084	0.009	0.762	49.25	0.493	0.059	88.89	55.56	1.1/14.4	
La_Jolla	50	0.128	0.023	0.112	0.015	0.670	54.86	0.774	0.042	52.00	32.00	28.4/16.2	
Lanai	46	0.105	0.014	0.073	0.007	0.621	55.59	0.699	0.053	80.44	47.83	2.9/2.2	
Rottneest_Island	46	0.069	0.012	0.053	0.004	0.226	61.42	0.195	0.059	89.13	71.74	2.2/–2.2	
UCSB	39	0.148	0.022	0.108	0.009	0.930	67.60	0.990	0.041	161.54	30.77	14.7/7.3	
San_Nicolas	29	0.115	0.018	0.067	0.004	0.755	107.30	0.839	0.059	51.72	24.14	0.0/–3.4	

Table 5. (continued)

Site	Count	MISR AOD		AERONET AOD		AOD Corr.	Mean Absolute Diff. (Rel. %)	AOD Gain	AOD Offset	AOD: 20%, or 0.05	AOD: 10%, or 0.03	DAOD: Surr. – Central <sup>b</sup>	V12 AOD: 20%, or 0.05/10%, or 0.03 <sup>b</sup>
		Mean	SD	Mean	SD								
<b>Hybrid_BD</b>	<b>614</b>	<b>0.346</b>	<b>0.053</b>	<b>0.372</b>	<b>0.019</b>	<b>0.876</b>	<b>36.80</b>	<b>0.597</b>	<b>0.124</b>	<b>47.56</b>	<b>27.85</b>	<b>–2.3/–0.7</b>	
Ouagadougou	66	0.347	0.041	0.427	0.021	0.907	20.84	0.553	0.111	59.09	33.33	–5.4/–2.0	
Bamako	142	0.425	0.066	0.460	0.023	0.855	21.77	0.659	0.122	63.38	45.07	0.5/–0.6	
DMN_Maine_So	41	0.351	0.060	0.351	0.027	0.846	21.91	0.722	0.097	70.73	41.46	–1.7/6.2	
IER_Cinzana	117	0.349	0.049	0.383	0.016	0.878	24.01	0.757	0.060	58.97	36.75	0.9/–0.9	
Djougou	29	0.501	0.057	0.712	0.031	0.905	29.17	0.618	0.061	27.59	13.79	–8.2/–10.6	
Ilorin	35	0.507	0.040	0.774	0.030	0.867	32.30	0.468	0.145	28.57	8.57	–3.6/2.5	
Sede_Boker	184	0.225	0.049	0.152	0.012	0.815	67.64	0.793	0.105	25.54	9.78	–3.7/–0.2	

<sup>a</sup>AERONET, Aerosol Robotic Network; Corr., correlation; Diff., difference; Rel., relative; SD, standard deviation. AERONET spectral AOD was interpolated to the MISR green-band wavelength for these comparisons (see text). The last column contains Version 12 (V12) results corresponding to the Biomass Burning, Continental, Dusty, and Maritime categories, though with a different selection of sites and different sampling, from Kahn *et al.* [2005a] (paper 1). These data are from the V22 aerosol product.

<sup>b</sup>This column contains two numbers. The first is the difference between the percentage of MISR [Central + Surroundings (Surr.)] falling within 0.05 or 20% × AOD of the corresponding AERONET value, and the percentage of MISR Central-only falling within this envelope. The second number is the same quantity, but calculated for the 0.03 or 10% × AOD envelope. For the categories overall (in boldface here), these quantities are plotted in Figure 2 along the vertical axis. See text for details.

bottom row); such situations, where SSA is not a leading factor in AOD underestimation, are discussed in the next section.

### 3.3. AOD Performance at Dusty, Continental, Urban, and Hybrid (Smoke + Dust) Sites

[40] Statistical AOD comparisons with AERONET at Dusty sites (Figure 2 and Table 5) yield results similar to those in previous studies [Martonchik *et al.*, 2004; Kahn *et al.*, 2005a; Kalashnikova and Kahn, 2006]. AOD discrepancies with ground truth are somewhat larger over bright desert surfaces than for other site categories, but the patterns of overall agreement, some overestimation for very low AODs and underestimation for high AODs, as shown in Figure 3, parallel those for the Biomass Burning sites discussed earlier. As the details of AOD retrieval success depend in part on the aerosol optical properties included in the algorithm, some limitations in the V22 component and mixture assumptions that can affect AOD results, such as those for dusty situations, are discussed further in section 4.

[41] For Continental sites Figure 2 and Table 5 show large differences from site to site in the level of AOD agreement between MISR and AERONET. This reflects the diversity of conditions in the Continental grouping; the sites cover an enormous range of surface fractional vegetation cover and locations where different mixtures of spherical and non-spherical aerosols dominate. Figure 3 shows that there are relatively few Continental cases for which the midvisible AOD exceeds about 0.6, because these sites tend to be away from sources that produce concentrated aerosol plumes. Again, the patterns of overall AOD agreement, overestimation for very low AODs and underestimation for AOD  $\geq 0.4$  (Figure 3, row 3) parallel those for other categories. However, unlike the smoke particles discussed in section 3.2, Continental aerosols often have SSA at or near unity, so at least one factor in addition to SSA must contribute to the observed underestimation at high AODs.

[42] As discussed by Chen *et al.* [2008], at higher AOD there is less signal from the surface, and in such circumstances the lack of surface information creates ambiguity that can result in the algorithm assigning too much of the TOA radiance to the surface (i.e., a higher surface albedo), thereby underestimating the AOD. But in principle, the surface reflectance adopted by the algorithm should matter less as the AOD increases, and the algorithm might partition the radiance in various ways when there is less information about the surface. However, variations in the AOD itself can produce scene variability that could be interpreted by the heterogeneous-land component of the MISR over-land algorithm as coming from the surface, leading to errors in the retrieved AOD in some situations.

[43] The AOD for the Continental category overall varies much less systematically with season than for the Biomass Burning and Dusty categories, owing in part to the greater site-to-site variability of aerosol source types for Continental cases, as well as the inherently seasonal nature of dust storm and fire occurrence. This seasonal behavior is not shown explicitly in the plots, but it is suggested by the degree to which the seasonal color coding is more stratified for the Dusty and Biomass Burning categories in Figure 3 than for Continental cases.



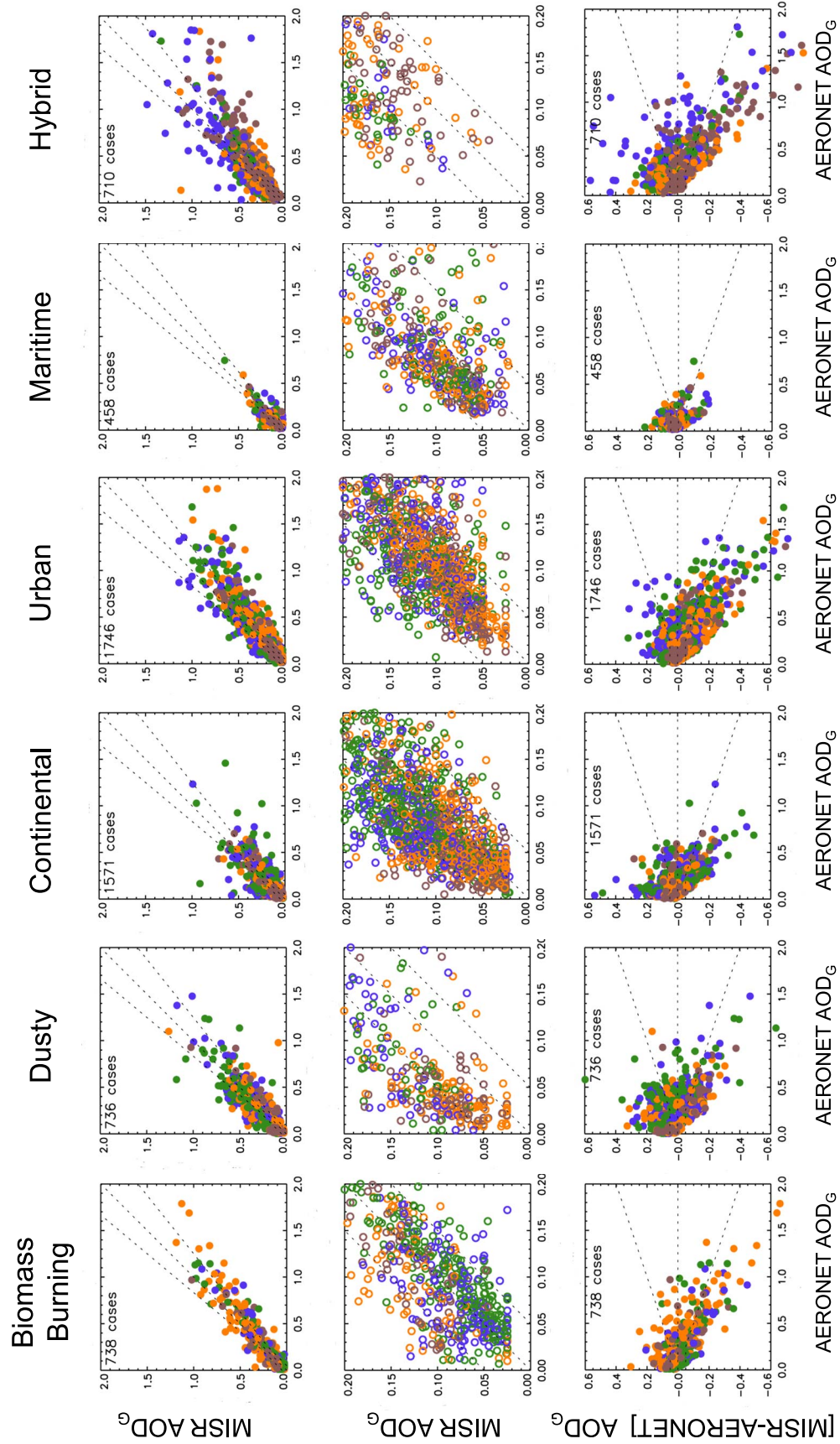
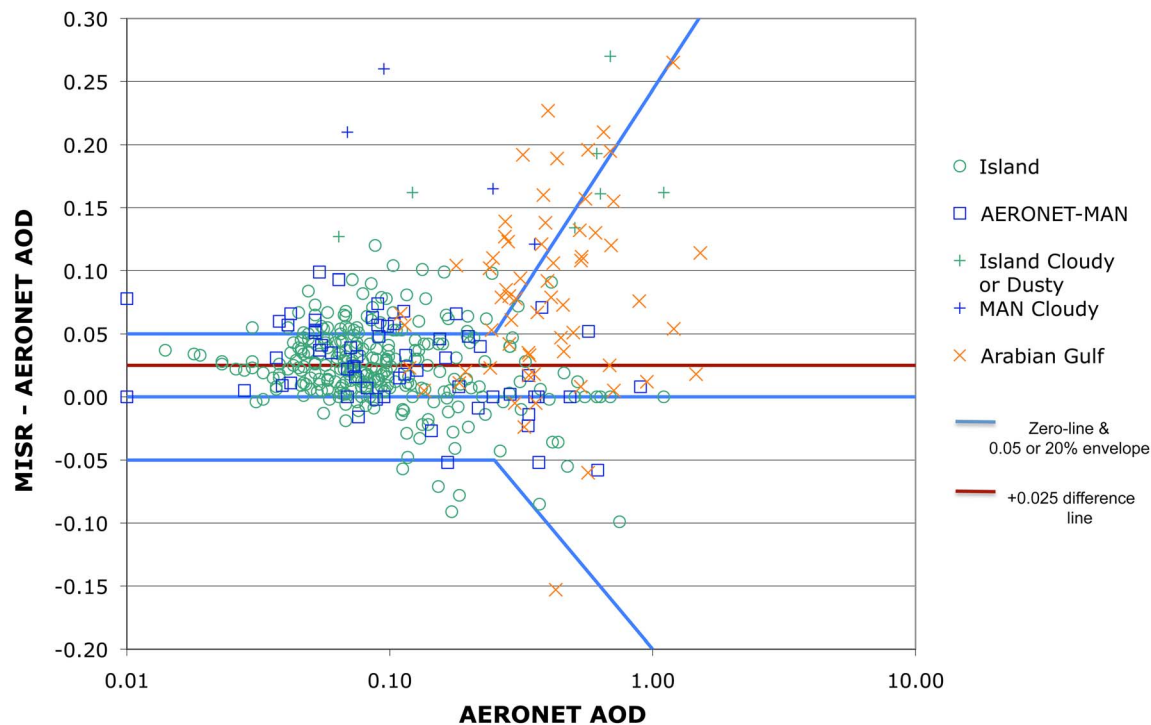


Figure 3



**Figure 4.** Difference plot showing comparisons between MISR over-water algorithm midvisible AOD retrieval results and near-coincident AERONET retrievals over island sites (open green circles) and ship-board, handheld Sun photometer observations (open blue squares) from AERONET's Marine Aerosol Network (MAN) [Smirnov *et al.*, 2009]. Green and blue crosses indicate scenes dominated by broken cloud or dust plumes, and orange exes identify AERONET sites in relatively shallow, polluted waters of the Arabian Gulf (Abu Al Bukhoosh and Sir Bu Nuair). AOD is used for the horizontal axis; blue lines mark the zero difference and bracket the 0.05 or  $20\% \times \text{AOD}$  envelope, and the red line marks the  $+0.025$  MISR AOD offset discussed in section 3.1.

[44] The MISR-AERONET AOD agreement for Urban sites in Figure 2 is similar to that for the Continental category, but the aerosol is more spatially localized. This favors MISR central retrieval regions, compared to MISR surrounding regions, as discussed at the beginning of section 3; it also leads to more frequent midvisible AOD values exceeding 0.6, as shown in Figure 3.

[45] The MISR AOD retrieval performance for the Hybrid aerosol air mass category was identified as problematic in earlier comparisons between MISR and AERONET (paper 1) and between MISR and MODIS, especially in sub-Saharan Africa, in southern Africa, and near Mexico City during certain seasons [Kahn *et al.*, 2009a]. Detailed analysis of individual cases by Chen *et al.* [2008] showed that seasonal mixing of spherical, absorbing smoke and nonspherical dust

is common in western Africa from December through March. In Figure 2 here, the MISR AOD retrievals in the Hybrid category again show the poorest statistical agreement with AERONET among the categories identified here. Taken together, these results reinforce the need to add mixtures of nonspherical dust with spherical, absorbing smoke particle analogs to the MISR standard retrieval climatology. Returning to Figure 3, the qualitative trends are similar to those observed for the other categories: where outliers occur, the MISR V22 product tends to overestimate low AOD values and underestimate high AOD values.

### 3.4. Global Distribution of AOD Outliers

[46] On a global basis the AERONET site distribution does not provide an adequate statistical assessment of AOD

**Figure 3.** (top row) Midvisible (558 nm) MISR vs. AERONET coincident AOD scatterplots, stratified based on the six broad aerosol type categories expected to dominate, at least during some seasons, at each site. Seasonality is represented by color: December–January–February (DJF), brown; March–April–May (MAM), blue; June–July–August (JJA), green; September–October–November (SON), orange. (middle row) Magnified versions of the top-row scatterplots, for AODs between 0 and 0.2, which reduces overplotting and helps clarify seasonality. (bottom row) (MISR – AERONET) vs. AERONET difference plots for the full set of midvisible coincident AOD data, stratified and color-coded as before. AERONET data have been interpolated to the MISR effective wavelength for all cases, and  $\text{AOD}_G$  represents AOD in the MISR green band. Dotted lines mark perfect agreement and the 0.05 or  $20\% \times \text{AOD}$  agreement envelopes. Statistics associated with these plots are listed in Table 5.

outlier geographical patterns. MISR and MODIS, both satellite remote-sensing instruments, do not carry the same weight as ground-based AERONET data for satellite AOD validation. However, comparisons between coincident MISR and MODIS/Terra AOD retrievals offer some useful insights in this regard [e.g., Kahn *et al.*, 2009a], so we take advantage of the much greater coincident coverage for the two Terra instruments to help fill the gap in our statistical assessment, offering a global view of locations where discrepancies occur. The comparison provides clues about places where systematic MISR algorithm issues might arise, but in themselves, they do not offer a definitive indication of the underlying causes.

[47] Figure 5 shows the geographical distributions of points for which the MISR-MODIS midvisible AOD discrepancies exceed 0.2 over land, and 0.125 over ocean, for January and July 2006. These outlier subsets represent 1% and 0.6% of the total population of coincidences over water for January and July 2006, respectively, and 10% and 6% for January and July 2006 over land. Here we associate observed outlier patterns with algorithmic factors that are likely to be involved. But aside from algorithm issues, actual differences in MISR-MODIS sampling, convolved with AOD variability at kilometer scales, contribute to the outlier populations as well, especially in high-AOD situations [e.g., Kahn *et al.*, 2007a, 2009a], and even in regions of outlier concentration, only a small fraction of coincident retrievals shows large discrepancies.

[48] Regionally, the outliers tend to cluster in places where known issues occur, as discussed by Kahn *et al.* [2009a]. Over land, the Sahel region of Africa stands out, as smoke and dust particles are mixed in the atmospheric column. MODIS aerosol optical models applied in this season and region include mixtures of smoke and dust particles [Remer *et al.*, 2005; Levy *et al.*, 2007], whereas V22 MISR aerosol models do not. Generally, the MISR AOD exceeds the MODIS value in these cases, as indicated by the difference-plot insets in Figures 5a and 5b. For eastern China, and for northern India in January, low-SSA pollution particles are common. The MISR AOD underestimation at high AODs, noted in sections 3.2 and 3.3, and the lack of retrieved low-SSA spherical particles in the MISR V22 product combine to produce in these regions some of the largest outliers in the over-land data, with MISR AODs lower than MODIS values. In July, wildfire smoke in Siberia and parts of the western United States produces similar effects, whereas smoke is sometimes mixed with dust over central Africa, so MISR-MODIS difference outliers of either sign occur in this region, though at high AODs, MISR underestimation tends to dominate. MODIS AOD overestimation over the bright land surfaces produces outliers for Patagonia in January, and this effect, along with MISR AOD underestimation at high AODs, generates scattered outliers in the western and central United States and Europe, especially in July.

[49] Over water, cloudy regions in the seasonal storm track bands produce most of the observed AOD differences; these appear preferentially in the Southern Ocean and across the northern midlatitude oceans in January and in the southern midlatitude oceans in July. Also in July, MISR-MODIS over-water AOD differences of either sign occur where cloud and some sea ice appear, at high northern latitudes; most often, MODIS is higher than MISR. The MODIS AOD also tends to

exceed the MISR value off the coast of western Africa in January and off the central African coast in July, places where high-AOD dust or smoke plumes, or smoke-dust mixtures, are common in these seasons.

[50] There is also a concentration of outliers of either sign in some coastal regions, such as along south Asia, the Red Sea, and the Arabian Gulf, especially in January. These regions correspond with relatively high concentrations of dissolved organic matter in the SeaWiFS satellite ocean-color data (not shown). As mentioned in section 3.1, the MISR and MODIS over-water algorithms assume a dark ocean surface at red and longer wavelengths; Kahn *et al.* [2007a] describe differences in the way these algorithms treat observed radiances in such situations that can account for the retrieved AOD discrepancies. Bright coastal (Case 2) water also contributes to, and in places might dominate, situations where over-water MISR and/or MODIS AOD retrievals are discontinuously higher than the corresponding results for nearby land.

#### 4. Particle Microphysical Property Retrieval Assessment

[51] Figure 6 offers a qualitative overview of MISR aerosol air-mass-type identification, based on the lowest residual mixtures retrieved for cases where AOD > 0.15. For situations where dust is most likely, mixtures containing nonspherical particles are especially common (mixtures 51–74; see Table 3). Where biomass burning smoke or urban pollution aerosol is expected, the retrievals tend to pick mixtures containing spherical, absorbing particles (mixtures 31–50). At some Maritime sites, transported dust or smoke is observed, though sampling in this category is poor in the MISR-AERONET coincident data, as discussed in section 3.1. Spherical absorbing and nonabsorbing particles, as well as nonspherical dust are all common at Continental, Urban, and Hybrid sites, but absorbing particles appear less frequently at Continental than at Urban and Hybrid sites, where aerosol containing black carbon from incomplete combustion is more likely to be found.

[52] Figure 7 presents a geographically oriented view of retrieved aerosol properties from the July 2007 MISR V22 aerosol product, in the same three broad categories highlighted in Figure 6: spherical nonabsorbing (cyan), spherical absorbing (magenta), and nonspherical (yellow). The MISR algorithm retrieves aerosol properties from a climatology of components and mixtures that is applied globally (Tables 2 and 3), rather than preselecting them based on region or season. Many expected patterns appear, such as nonspherical dust analogs over and downwind of North African and Middle Eastern desert dust sources. Spherical, absorbing smoke analogs are retrieved in tropical and boreal summertime biomass burning regions, and similar particle types are found around pollution centers along the east coasts of North America and China, whereas spherical, nonabsorbing maritime particles are retrieved over much of the Southern Hemisphere oceans.

[53] Some artifacts appear as well, especially in remote-ocean and other low-AOD regions where sensitivity to particle properties is reduced. Nonspherical particles are retrieved at times over equatorial, Southern Hemisphere, and some boreal waters that are likely to be unscreened cirrus



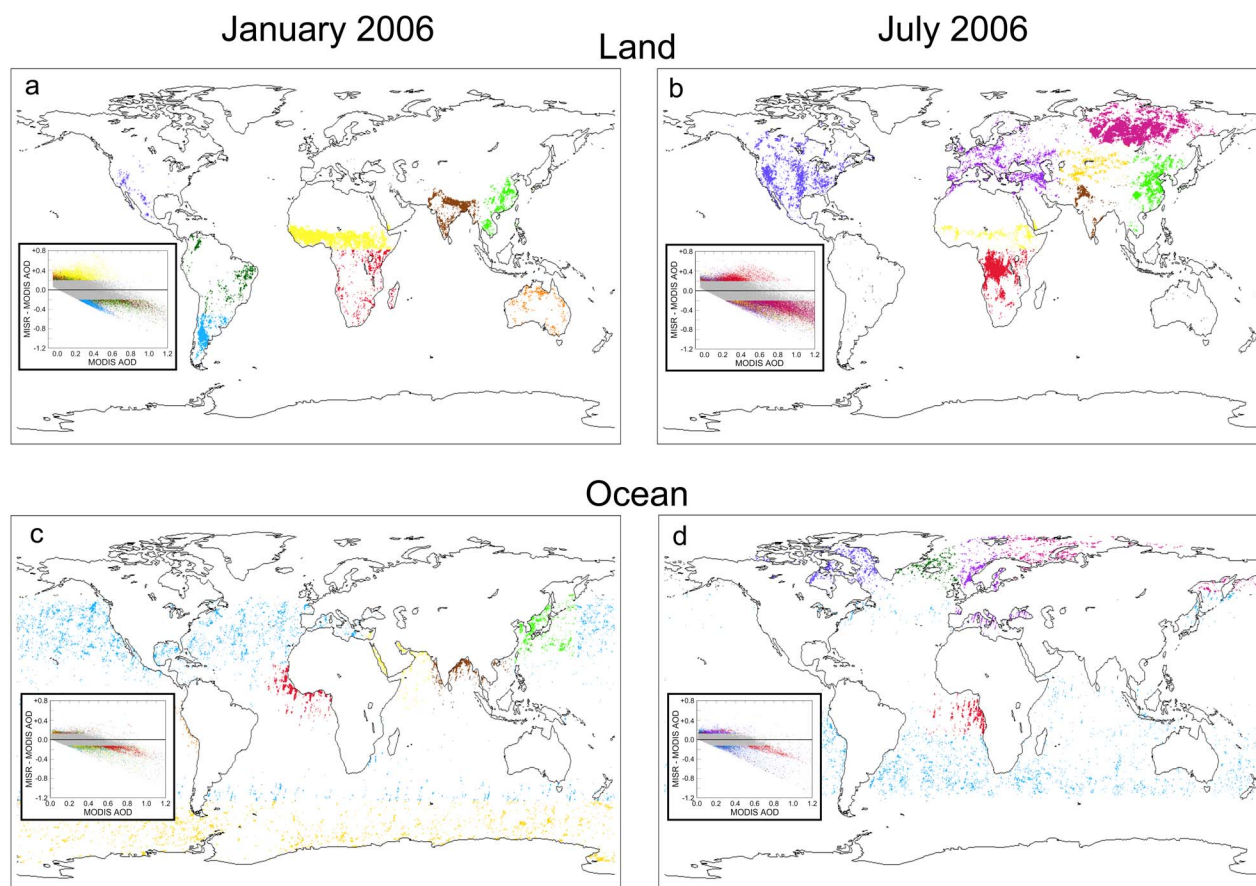


**Figure 5.** MISR-MODIS outliers. Geographical distributions of coincident MISR and MODIS AOD retrieval cases where the  $\text{abs}(\text{MISR\_AOD} - \text{MODIS\_AOD})$  is  $>0.125$  for over-ocean plots and  $>0.2$  for over-land plots, color-coded by region. (a) January 2006 over land; (b) July 2006 over land; (c) January 2006 over ocean; (d) July 2006 over ocean. (insets) Difference plots of  $(\text{MISR\_AOD} - \text{MODIS\_AOD})$  vs. MODIS AOD, color-coded with the same scheme as the respective maps, but overplotted, so some information is lost where the data overlap.

[Pierce *et al.*, 2010]. Absorbing, spherical particles are frequently retrieved over Northern Hemisphere oceans in the July map and shift to the Southern Hemisphere oceans for January 2007 (not shown). In these regions the range of scattering angles viewed by MISR, and hence the sensitivity to particle type, is limited in summer [Kahn *et al.*, 1997, Figure 2].

#### 4.1. Angstrom Exponent

[54] In this section we go beyond the broad, qualitative assessments, by comparing MISR and AERONET ANG differences as a function of AERONET AOD, for Biomass Burning, Dusty, and Continental sites, stratified by season (Figure 8). The difference plots provide a more sensitive representation of deviations than the scatterplots that are often used for such comparisons. Smaller dots identify cases where the AOD is below 0.15, and arrows highlight some of the low-AOD situations where the MISR ANG values are especially scattered, relative to AERONET values. As discussed in previous papers (e.g., paper 1), this is expected; particle microphysical property information is reduced when the AOD is below about 0.15 or 0.2, depending on conditions, owing to increased relative contributions from surface

reflectance uncertainties, unmasked cloud, etc. However, as a consequence of the systematic air-mass factor sampling that MISR multiangle views provide, MISR AOD retrievals themselves tend to be robust down to values of 0.05 or lower even when particle microphysical properties are poorly constrained [e.g., Kahn *et al.*, 1998, paper 1].

[55] Most of the biomass burning cases in this data set occur during northern summer and autumn. As Figures 8c and 8d illustrate, the MISR-retrieved ANG values scatter fairly uniformly around the zero-difference line during these seasons when the AOD is between 0.15 and about 0.6. However, as already noted, the range of spherical particle size and SSA combinations in the V22 retrieval algorithm is limited; a richer set of components and mixtures would reduce the observed scatter and should improve the ANG underestimation at higher AODs (see section 4.2). This has been demonstrated with the MISR research aerosol retrieval algorithm for individual cases [e.g., Chen *et al.*, 2008], but for implementation in the standard algorithm, accommodation must also be made for situations where particle property information in the observations is limited (see section 5). Figure 8e displays the MISR-AERONET ANG difference as a function of the AERONET ANG for Biomass Burning

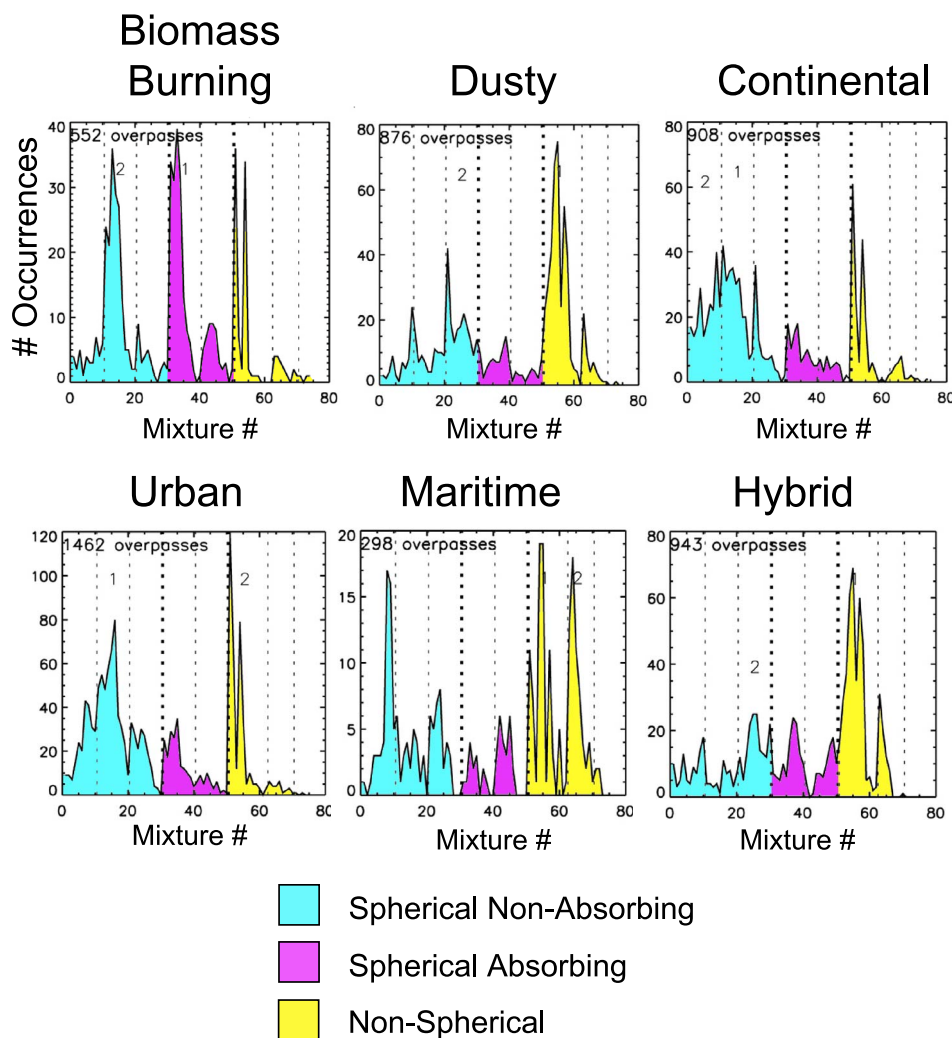


**Figure 6.** MISR-retrieved aerosol types. Histograms show the number of lowest-residual occurrences of each aerosol mixture, for all events within the MISR-AERONET coincident event data set having a mid-visible MISR AOD > 0.15. Data are stratified by sites where each of the six broad aerosol air-mass type categories is expected, at least in some seasons. Attempts at further stratification by aerosol air-mass type proved unhelpful, owing to site-to-site differences in seasonality, interannual variability, and limited event-by-event aerosol type information. Mixture definitions are listed in Table 3, and histograms are color-coded to identify mixtures containing spherical, nonabsorbing particles of various sizes, those that include spherical absorbing particles, and mixtures containing nonspherical dust along with spherical components. The same color scheme is used in Figure 7. Note that the vertical scales vary from plot to plot, depending on the available sample size.

sites. Although the vast majority of points in Figure 8e are overplotted close to the zero-ANG-difference line (easier to see in Figures 8a–8d), the outliers show a tendency for MISR to overestimate the ANG when the AERONET ground-truth ANG value is small and, conversely, to underestimate the ANG when it is large. That is, the dynamic range of the MISR-retrieved ANG is less than that of the AERONET ANG, further indicating that a richer set of spherical components and mixtures could improve the results.

[56] Dust events in this data set are most common during northern spring and summer. Figures 8g and 8h show that the MISR V22 algorithm systematically overestimates the ANG at sites frequently dominated by desert dust when the AOD > 0.15, indicating that the particles retrieved by MISR under

dusty conditions tend to be smaller than those observed by AERONET. Figure 8j illustrates more specifically that when the AERONET ANG < 1 (i.e., when medium to large particles dominate), MISR retrieves smaller particles (larger ANG). Several factors likely contribute to this trend. The MISR algorithm contains only two nonspherical components, one medium- and one coarse-mode aerosol analog (Table 2); the coarse-mode optical model, generated from a distribution of ellipsoids, does not provide a completely satisfactory match to thick or near-source dust plumes observed by MISR, even when combined with medium-mode dust [Kalashnikova and Kahn, 2006]. Developing more generally applicable coarse-mode dust optical models is the subject of current research [e.g., Bi et al., 2010]. In addition, owing to the lack of



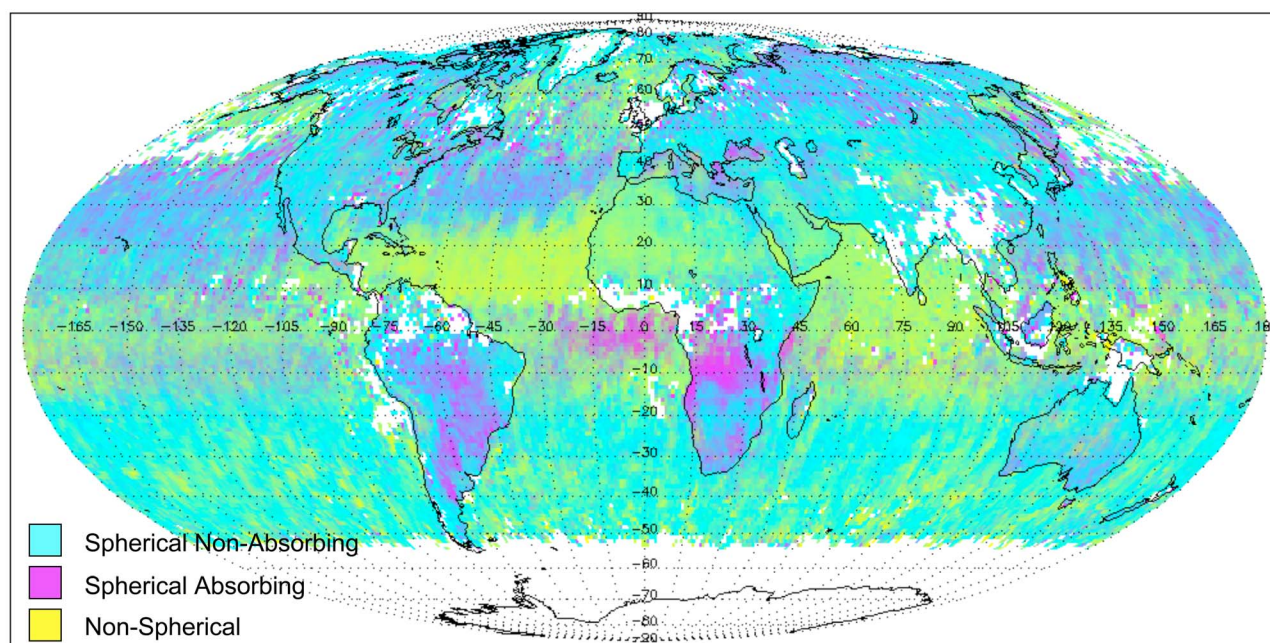


**Figure 7.** Global map showing the distribution of retrieved spherical nonabsorbing, spherical absorbing, and nonspherical components, for the July 2007 MISR V22 aerosol product. In each  $1^\circ \times 1^\circ$  bin, the lowest-residual mixtures are considered. The fraction AOD of all spherical nonabsorbing components in the lowest-residual mixture is multiplied by the retrieved AOD for each observation, summed for the entire month, and assigned the cyan color. Fractions of spherical absorbing and nonspherical components are processed similarly and assigned magenta and yellow, respectively. Linear, ternary mixing is used to assign the overall color to the  $1^\circ \times 1^\circ$  bin, with pure cyan, magenta, and yellow as the three end members. AOD weighting de-emphasizes the low-AOD retrievals for which the retrieved particle properties are less certain. Retrieved aerosol properties reflect many of the expected regional-scale patterns as well as some artifacts, as discussed in the text.

spectral channels longer than 866 nm, MISR is insensitive to the optical properties of coarse-mode particles larger than about  $2.5 \mu\text{m}$  in diameter, whereas desert dust aerosol distributions often contain a significant fraction of particles up to about  $10 \mu\text{m}$  in size, especially near sources.

[57] According to Figure 8 there is also a tendency for the MISR retrievals to overestimate the ANG at Continental sites, and the ANG dynamic range is again smaller than that obtained by AERONET (Figure 8o), further indicating the need for a richer set of components and mixtures in the retrieval climatology. In particular, the effective radius of the “large spherical” particle among the V22 aerosol components is  $2.80 \mu\text{m}$  (particle 6 in Table 2), and the next-smaller spherical particles are  $0.26$  and  $0.12 \mu\text{m}$  in size (particles 3 and 2, respectively). Absorbing spherical particles are available only at a  $0.12 \mu\text{m}$  effective radius in V22 (particles 8 and 14). Given the limited mixtures available in V22, for situations where the retrieved ANG is too high, the MISR algorithm often picks a combination of unduly small particles, along with enough very large particles to match the observed radiances as much as possible.

[58] Field data indicate that particles of sizes intermediate between those of particles 3 and 6 are significant in some regions. The AERONET climatology is dominated by a “fine-mode” component having very nearly the size distribution of particle 2 (Table 2) for all aerosol type cate-

gories and a “coarse-mode” component that is much more variable, but with a midrange close to that of MISR particle 6 ([Dubovik *et al.*, 2002]; to compare this reference with Table 2 here, the AERONET particle size parameters were converted from volume-weighted to number-weighted log-normal distribution values). However, even though the AERONET data are often interpreted in terms of bimodal distributions by fitting their 22 size bins with two log-normal distributions, particles having effective radii between  $0.26$  and  $2.8 \mu\text{m}$ , or even an additional mode in this size range, appear in the underlying retrievals in some cases. Examples include Cape Verde, the Maldives, and possibly Bahrain [Dubovik *et al.*, 2002, Figure 1], based on AERONET V1 processing, and at Ilorin in West Africa [Eck *et al.*, 2010] with the more robust V2 processing. More generally, spherical particles having sizes between the  $0.26$  and the  $2.80 \mu\text{m}$  V22 MISR components can form as combustion and biomass burning particles age, for example, downwind of the east coasts of North America and China. These regions are not well sampled by AERONET stations but contribute significantly to satellite data records having global coverage.

#### 4.2. Constraints on Particle Size as a Categorical Variable

[59] Spherical-particle sensitivity studies using a fine grid of spherical particle sizes, and SSA values indicate that, in

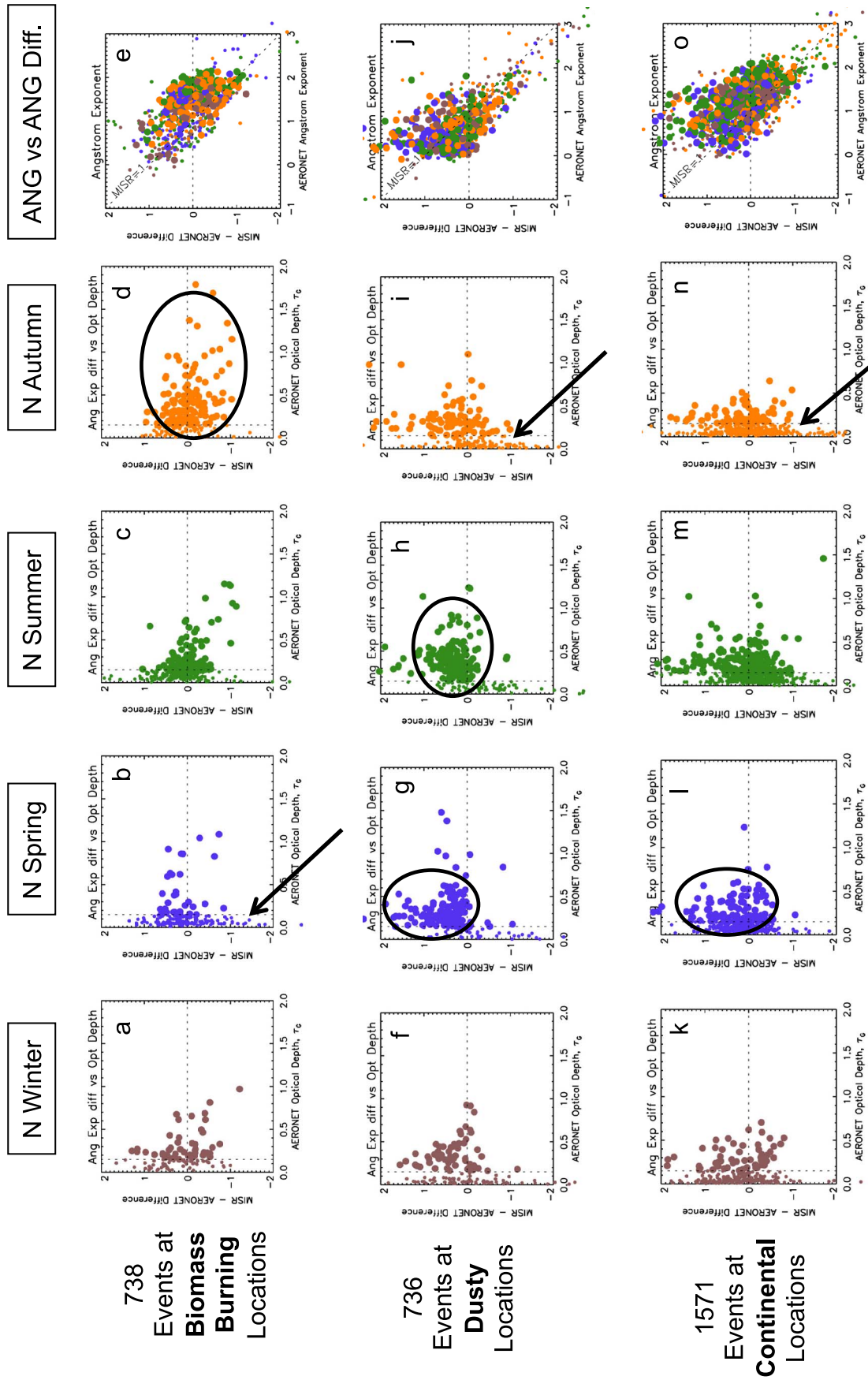


Figure 8



general, MISR can separate three to five size groupings under good retrieval conditions, that is, when the midvisible AOD is  $\geq 0.15$  or 0.2, with minimal cloud, surface snow and ice, or whitecap contamination, and for relatively uniform aerosol loading on 1 to 10 km scales [Kahn *et al.*, 1998; Chen *et al.*, 2008]. As such, particle sizes intermediate between the “coarse” ( $2.8 \mu\text{m}$ ) and the “fine” ( $0.12$  or  $0.26 \mu\text{m}$ ) effective radius modes, discussed in section 4.1, can be distinguished from the MISR data. The sensitivity studies also showed that particle size, as retrieved by MISR, should be treated as a categorical rather than a continuous variable, providing an aerosol type *classification* amounting to small, medium, and large.

[60] This classification is reflected in the MISR aerosol product variable Regional Best-Estimate Spectral Optical Depth Fraction (RegBestEstimateSpectralOptDepthFraction), which reports the fraction of the total column AOD assigned to particles having radii  $<0.35 \mu\text{m}$  (small),  $0.35$  to  $0.70 \mu\text{m}$  (medium), and  $>0.70 \mu\text{m}$  (large). The classification is based on the sensitivity studies cited previously and on the V12 algorithm, which included intermediate-sized particles having effective radii of  $0.57$  and  $1.28 \mu\text{m}$  (paper 1).

[61] To assess MISR-retrieved particle size as a categorical variable, we applied  $k$ -means cluster analysis to the MISR vs. AERONET ANG values. The AERONET ANG values are obtained from direct-sun measurements and provide a reliable and well-sampled ground-truth quantity (see section 2.1), whereas AERONET size distributions are derived with additional assumptions. We subsequently interpret the comparative ANG values in terms of the MISR-retrieved mixtures and components.

[62] The clustering approach determines bins or “clusters” directly from the data, rather than imposing them arbitrarily, as must be done, for example, to create two-dimensional histograms showing MISR vs. AERONET ANG. The cluster analysis thus allows for a more critical analysis of actual MISR V22 ANG performance, which is required to assess the underlying causes of discrepancies. The algorithm used begins with  $k$  “seeds,” constituting an initial guess at the number and centroid values of the clusters. Using a distance metric, the algorithm identifies all points that are closer to a given seed than any other, and calculates the centroid of all points associated with each seed. These centroids are then taken as the new seeds, and the process is iterated until convergence [e.g., Press *et al.*, 2007]. This approach allows us to determine the number and range of ANG classes in the data and to evaluate their degree of separation. The number of categories that the data can distinguish is obtained as the highest value of  $k$  that produces separable clusters arrayed near the 1:1 line in a plot of retrieved vs. validation ANG data. We used the simple Euclidean distance as our metric and performed the cluster analysis for  $k$  values of 2, 3, 4, and 5 on the coincident MISR-AERONET ANG pairs for each of the six aerosol type cat-

egories. Several initial seed locations were tested in each case, to assure the robustness of the results.

[63] The plots in row 1 in Figure 9 show the results for  $k = 3$ ; that is, the algorithm was initiated with three cluster seeds, which are marked as open black circles. The centroids of the final clusters, shown as filled black circles in these plots, are systematic and fall roughly along the 1:1 line for the Maritime category. For the Urban, Continental, Hybrid, and Biomass Burning classes, two of the three point clouds are less separable when projected along the vertical (MISR ANG) axis. The clusters are more systematic for  $k = 2$  and become increasingly scattered for  $k = 4$  and  $k = 5$  (not shown). To help interpret these results in terms of what they say about the particle types available in the V22 algorithm, Figure 9 also shows, in row 2, scatterplots of AOD (format similar to Figure 3) and, in rows 3–5, histograms of all successful mixtures in the retrievals (format similar to Figure 6) for each of the three clusters, respectively. These plots are color-coded by the clusters identified in the row 1 plots. As expected, the large particle clusters (green; small ANG) are associated with systematically higher AODs for the Dusty and Hybrid categories shown in row 2, whereas the small and medium particle clusters (orange and purple) tend to have higher AODs for sites often dominated by Biomass Burning smoke; the situation for Continental and Urban sites is more mixed.

[64] The Figure 9 data confirm, and add specificity to, many expected patterns in particle size and, more generally, in particle type (e.g., Figure 7). In Figure 9, row 3, the preponderance of small, absorbing smoke particles stands out in the Biomass Burning and Hybrid categories (mixtures 31–36 and 41–45; Table 3), and their occurrence at times in the other categories is also evident. Spherical non-absorbing particles are common in all categories, especially mixtures 11–18, containing the small to medium particle ( $0.12 \mu\text{m}$  effective radius) that is also the fine-mode size distribution preferred by AERONET; it is mixed with up to 60% midvisible AOD of the very large spherical component (particle 6), the common coarse-mode component of the AERONET climatology. In the Dusty and Hybrid categories, mixtures containing fine-mode spherical-absorbing particles along with significant fractions of the very large, spherical particle 6 are also common.

[65] Considering next the clusters of low ANG and larger effective particle size represented in rows 4 and 5 of Figure 9, the peaks progressively broaden in all categories except Dusty, moving toward greater admixtures of the very large spherical particles within each 10 mixture grouping of the MISR algorithm climatology (Table 3), as would be expected. Medium dust is more common, and coarse dust (mixtures 63–74), which is nearly absent from the row 3 clusters, makes significant contributions to most categories. Note that for the Continental and Urban categories, the respective mixture spectra in rows 4 and 5 are very similar

**Figure 8.** (MISR – AERONET) Angstrom exponent (ANG) vs. AERONET AOD is shown in rows 1 through 3 for locations dominated, at least during some seasons, by (a–d) Biomass Burning, (f–i) Dusty, and (k–n) Continental aerosol air-mass types. Columns are distinguished by season. Column 5 provides the annual aggregate of (MISR – AERONET) ANG vs. AERONET ANG for the respective categories. Smaller circles are for cases where the AERONET AOD  $< 0.15$ . Zero-difference lines are indicated by dashed horizontal lines, and dashed vertical lines mark AERONET AOD = 0.15 in plots in the first four columns. For plots in the fifth column, the MISR ANG = 1 line is drawn.

for all mixture groupings, and for Biomass Burning the main difference is a shift between small, spherical particles having different SSA values. This demonstrates why the purple and green (medium and small ANG) clusters for these categories in row 1 (Figure 9) have poorly resolved ANG values in the MISR data, despite having significantly different values in the AERONET data. Field-measured size distributions and previous MISR sensitivity studies suggest that adding to the mixtures in Table 3 components intermediate in size between the small to medium spherical particle 3 and the very large spherical particle 6 should move the centroids of the green clusters toward smaller ANG values, achieving closer agreement with the AERONET ANG ground truth. The same would also apply to the Biomass Burning and Hybrid categories, except that here, absorbing particles larger than  $0.12\ \mu\text{m}$  in effective radius would be needed [Chen *et al.*, 2008].

[66] The situation with the Dusty category is more complex. The MISR ANG values corresponding to the highest AERONET ANG values are too small; there are not adequate mixtures of dust with a medium-mode spherical particle, so mixtures of medium dust with the large spherical particle 6 and mixtures of small absorbing (especially row 4 in Figure 9) and nonabsorbing (especially row 5) spherical particles with particle 6 are often selected. In part, particle 6 is substituting for dust, as there are few alternative mixture options in the V22 climatology, and in addition, the current coarse-mode dust optical model does not match the MISR data well [Kalashnikova and Kahn, 2006].

[67] In summary, AERONET provides a powerful tool for validating the ANG. When sufficient component and mixture options are available, the MISR algorithm distinguishes at least three groupings in ANG values, but detailed analysis also highlights specific limitations in the current component and mixture tables and, in particular, a lack of particles between  $0.26$  and  $2.8\ \mu\text{m}$  in effective radius.

#### 4.3. Particle Single-Scattering Albedo and Particle Sphericity

[68] For MISR, particle SSA and shape are also categorical variables; sensitivity analyses and early validation studies indicate that two to four groupings in SSA, and at least spherical vs. nonspherical shape, can be distinguished under good retrieval conditions (as defined in section 4.2) [Kahn *et al.*, 1997, 1998; Kalashnikova and Kahn, 2006; Chen *et al.*, 2008].

[69] We attempted to validate MISR-retrieved SSAs with AERONET, but there were too few coincident events meeting the AERONET high-AOD and low-solar-elevation-angle acceptance criteria to obtain a statistical sampling of SSA retrievals. The cases obtained are not representative of average conditions, though AERONET SSA values in general provide the most extensive suborbital coverage available.

[70] Qualitatively, MISR tends to obtain SSAs at or near unity, especially when the AOD is too low for MISR to produce good SSA constraints. Globally, sea salt and sulfate aerosols are nonabsorbing, and in addition, aged smoke and some pollution particles are only weakly absorbing, so this is a reasonable value to adopt in these circumstances. As discussed earlier, MISR does tend to retrieve absorbing particles preferentially at Biomass Burning and Hybrid sites in seasons when smoke is expected (Figures 6 and 7).

[71] Even with the limited particle component and mixture options available in V22, the MISR-retrieved SSA helps to distinguish aerosol air-mass types, especially when combined with retrieved particle size and shape information, as demonstrated statistically at the beginning of section 4, and in available field campaign events, where coincident sub-orbital measurements of the key validation quantities were made [e.g., Kahn *et al.*, 2009b, Figure 6].

[72] Validating MISR-retrieved particle shape is also challenging, again because ground truth is difficult to obtain. Although information on particle sphericity can be derived from AERONET sky-scan data [Dubovik *et al.*, 2006], the nonspherical AOD fraction is not yet provided as a validated field in the AERONET products. Individual cases where other coincident aircraft or surface field observations were obtained provide some additional tests of the retrieval results [e.g., Kalashnikova and Kahn, 2006; Kahn *et al.*, 2009b; Schladits *et al.*, 2009], and the evolution of the MISR-retrieved fraction AOD spherical for dust plumes during transport over ocean follows expected patterns [Kalashnikova and Kahn, 2008]. The MISR-retrieved particle shape also helps distinguish dust from spherical particles for air quality applications [Liu *et al.*, 2007a, 2007b], contributes to mapping changes in the seasonal distribution of anthropogenic vs. natural aerosols over India [Dey and Di Girolamo, 2010], and discriminates among thin cirrus, spherical particles, and, to some extent, dust over ocean [Pierce *et al.*, 2010]. In each of these studies, further validation of the MISR-retrieved particle properties specific to the application was performed, offering qualitative support for the MISR particle sphericity retrieval results, as do Figures 6 and 7 here.

### 5. Summary of Recommendations

[73] The MISR-AERONET coincident data set developed and analyzed in this paper adds to earlier product validation statistical comparisons having smaller samplings and to field campaign and other case studies. The effort has allowed us to take a detailed and critical look at the MISR V22 aerosol products, with the aim of assessing strengths and identifying specific areas where further improvements are possible. In this section we summarize the issues identified and suggest ways of addressing some of them in future aerosol product versions. Bear in mind that most of these issues affect small fractions of the data set and are confined to specific retrieval situations, geographical regions, and, in some cases, seasons. Overall AOD performance, in a global context, is summarized in section 6, which follows.

[74] 1. There is a *gap in MISR-retrieved midvisible AOD values below about 0.02*, as well as *quantization noise at 0.025 AOD intervals* reported previously from MISR-MODIS AOD comparisons. The gap tends to skew the retrieved AOD to higher values and is especially significant statistically for very low AOD situations, which dominate the Maritime category. This is also likely to contribute to adjacent land-ocean AOD differences, which tend to show higher AOD over ocean in some regions. The numerical scheme in future versions of the algorithm will correct these issues.

[75] 2. There is a *lack of medium spherical particles* in the V22 climatology, having effective radii between  $0.26$  and  $2.8\ \mu\text{m}$ . This tends to skew the retrieved ANG to larger values (smaller particles) in some situations. On the basis of

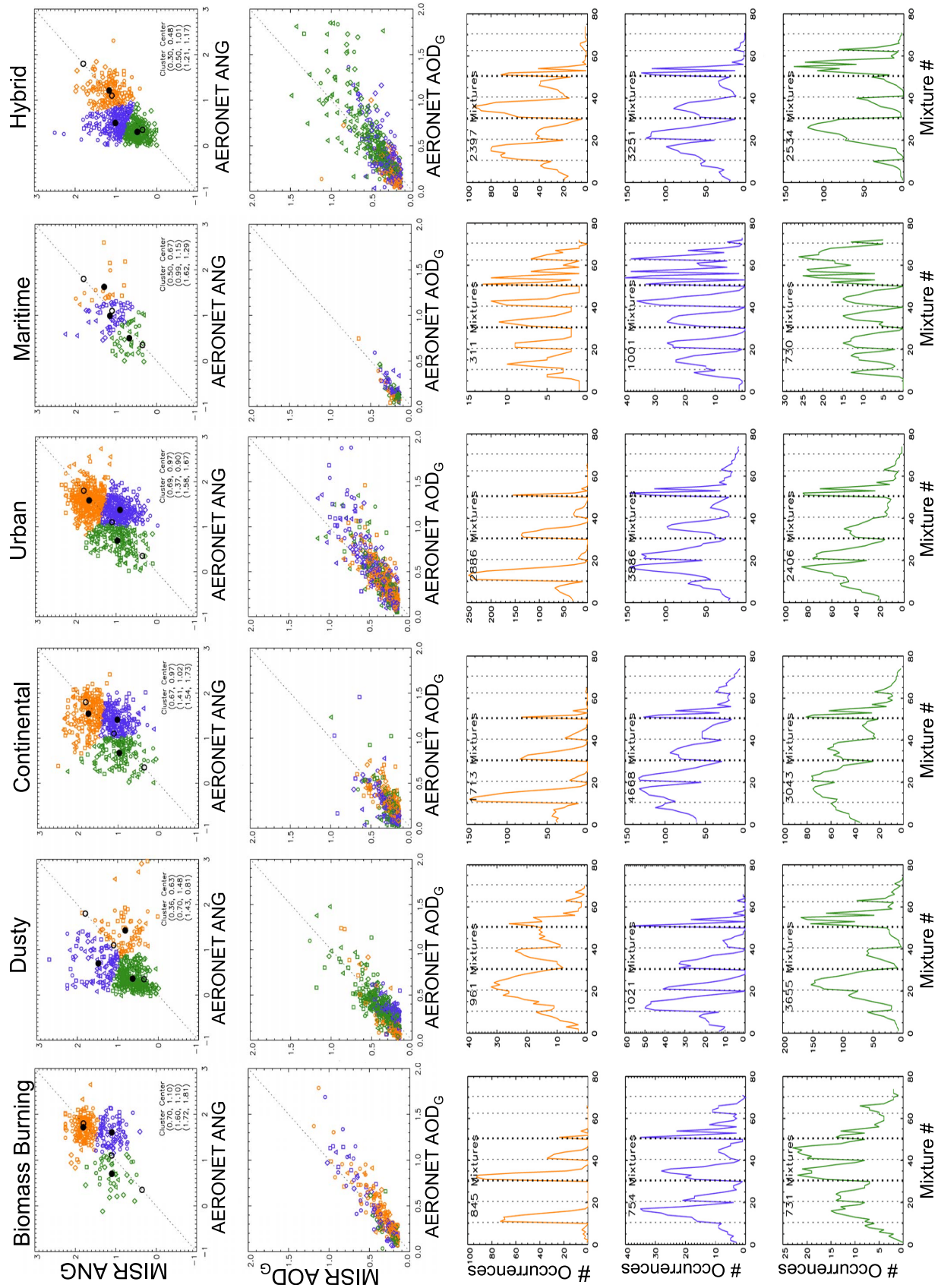


Figure 9

field observations, the addition of mixtures containing spherical nonabsorbing and, also, weakly absorbing (midvisible SSA  $\sim 0.94$ ) particles having an effective radius of about  $0.57 \mu\text{m}$ , as well as a spherical nonabsorbing component at about  $1.25 \mu\text{m}$ , should address this issue at the level of detail appropriate for typical MISR sensitivity.

[76] 3. There is a *lack of spherical, absorbing particles* in the V22 climatology at sizes other than  $0.12 \mu\text{m}$  effective radius. This tends to skew the retrieved AOD to lower values when absorbing spherical particles are present, as the algorithm sometimes selects spherical nonabsorbing particles closer to the AERONET-observed size range. The issue is most common for the Biomass Burning and Urban categories. On the basis of field measurements, the addition of spherical absorbing and weakly absorbing particles (midvisible SSA of about 0.84 and 0.94, respectively) having an effective radius of about  $0.06 \mu\text{m}$  and weakly absorbing particles having an effective radius of about  $0.26 \mu\text{m}$ , should address this issue [e.g., *Chen et al.*, 2008; *Dubovik et al.*, 2002]. Adjusting the SSA of the spherical absorbing and weakly absorbing  $0.12 \mu\text{m}$  particles in the current algorithm (Table 2) to these values could also improve the situation. The spectral dependence of SSA represents an additional dimension to be considered, as Urban Pollution particles generally have a shallower spectral slope than Biomass Burning particles [e.g., *Reid et al.*, 2005; *Bond and Bergstrom*, 2006; *Chen et al.*, 2008].

[77] 4. For an AERONET  $\text{AOD} \geq 0.4$ , the MISR-retrieved AOD is frequently underestimated over land (Figure 3), and possibly also over water, although the number of samples over dark, cloud-free water is too small to draw a strong conclusion (Figure 4). Several factors appear to be involved. (a) In situations where the atmospheric particles are absorbing, MISR tends to adopt an SSA at or near unity owing to a lack of absorbing, spherical particles in the V22 climatology. This skews the retrieved AOD low [*Kahn et al.*, 2005a, 2007a; *Chen et al.*, 2008]. (b) Most high-AOD underestimation cases occur when the actual particle SSA is at or near unity, so MISR SSA overestimation is not a factor. As the MISR heterogeneous-land component of the over-land algorithm assumes that TOA reflectance variability on 1 to 10 kilometer scales comes entirely from the surface [e.g., *Martonchik et al.*, 2009], AOD variability on these scales [e.g., *Redemann et al.*, 2006] could be assigned to the surface, causing an AOD underestimation. Unlike surface reflectance variability, the contributions of aerosol variations to the scene tend to increase with increasing view angle, which could be used to identify and flag such situations. Similarly, testing whether the MISR-retrieved

surface angular reflection factors differ significantly from location-specific values in a climatology derived from low-AOD MISR observations could be used for this purpose. (c) Other algorithmic factors are also under investigation by the MISR team.

[78] 5. There is a *lack of mixtures containing both spherical, absorbing smoke analogs and nonspherical dust* in the V22 climatology. This results in a poor AOD performance for the Hybrid category. Theoretical sensitivity analysis suggests that two-component mixtures in 10% or 20% AOD increments would capture the information content of the MISR data under good retrieval conditions [*Kahn et al.*, 2001; *Chen et al.*, 2008].

[79] 6. In the V22 algorithm, ANG in the Dusty category tends to be overestimated. As discussed by *Kalashnikova and Kahn* [2006], an upgraded coarse-mode dust optical analog should improve ANG, and to some extent AOD retrievals, when dust dominates the aerosol air mass, especially near dust source regions. The inclusion of medium spherical particles in the algorithm climatology seems likely to help reduce this discrepancy too, as discussed in section 4.

[80] 7. In situations where the range of scattering angles observed by MISR is diminished by solar geometry and sun glint over water, and/or when the midvisible AOD is below about 0.15 or 0.2, particle property information is diminished, and absorbing spherical particles are sometimes retrieved where none are expected. Flagging cases having low AOD or limited scattering angle coverage or, more generally, cases where many mixtures pass the algorithm acceptance criteria, would alert users to the possibility that particle property information in the observations is limited. Similarly, coastal water sites, where seasonally high runoff or ocean biological activity can increase ocean surface reflectance, and other regions and seasons where algorithm assumptions tend to be violated (Figure 5) can be flagged as a warning that retrieved AODs might be aliased.

## 6. Conclusions

[81] We have assessed the MISR V22 AOD and ANG products with coincident AERONET sun photometer observations from around the globe and have examined qualitatively MISR-retrieved SSA and fraction AOD spherical. Comparisons were stratified by season and by location; AERONET sites having good measurement records over the MISR observing period were partitioned into six categories, based on expected aerosol air-mass type. One challenge facing the validation effort, and the interpretation of MISR (and other) remote-sensing products, is that retrieval sensitivity varies

**Figure 9.** ANG cluster analysis. Row 1 presents MISR vs. AERONET ANG scatterplots, partitioned into  $k$ -means clusters, with  $k = 3$ , for each of the six aerosol air-mass type categories. Initial cluster seeds are shown as open circles, and final cluster centers are indicated as filled black circles; quantitative cluster centroid locations are given in the annotation in each plot. Row 2 shows the corresponding MISR vs. AERONET AOD scatterplots, colored according to cluster. Seasonal information is encoded in the symbol shapes: DJF, diamonds; MAM, triangles; JJA, squares; SON, circles. Rows 3–5 provide histograms of mixture number (Table 3) for all successful mixtures, similar in format to those in Figure 6 but partitioned and color-coded according to cluster, for ANG clusters identified with smaller (orange), intermediate (purple), and larger (green) column-effective particle sizes, respectively. Only cases having an MISR AOD  $> 0.15$  are included in this analysis, owing to the limited MISR aerosol property sensitivity for lower AODs, as illustrated in Figure 8; this accounts for the horizontal low-end cutoff in the AOD plots in row 2. Note that the vertical scales in the row 3–5 plots vary, based on the numbers of counts in each cluster.

considerably depending on environmental conditions, which include AOD, surface brightness, scene heterogeneity, range of scattering angles observed, and actual aerosol components in the column. The variation in sensitivity to particle properties has implications for the retrieval algorithm itself; the range of aerosol components and mixtures selected for the retrieval climatology represents a compromise between conciseness, to limit redundancy and reduce algorithm run time, and completeness, to capture the information content of the measurements under the best retrieval conditions.

[82] Overall, about 70% to 75% of MISR AOD retrievals fall within 0.05 or 20%  $\times$  AOD of the paired validation data, and about 50% to 55% meet the 0.03 or 10%  $\times$  AOD criterion, except in the Dusty and Hybrid (smoke + dust) categories. Substantially improved agreement compared to the early postlaunch assessment [Kahn et al., 2005a] was achieved for the Maritime and Biomass Burning categories (Figure 2), mostly owing to calibration adjustments and the addition of spherical absorbing aerosol components, respectively, made after the 2005 assessment.

[83] Scene heterogeneity makes an important contribution to MISR-AERONET AOD discrepancies. Sampling differences rather than retrieval error contribute to more than 80% of significant outliers in the paired MISR-AERONET data set (3.7% of all coincident cases). For the Maritime, Continental, and Dusty categories, averaging MISR retrievals covering a  $\sim 50$  km spatial scale provides systematically better agreement with the AERONET  $\pm 1$  h time series than comparing them with only the central 17.6 km MISR retrieval region containing the AERONET site. For the Urban category, persistent small-spatial-scale variability produces a statistical advantage when only the central MISR retrieval region is considered. As expected, the largest seasonal variability was found at most sites designated Biomass Burning or Dusty.

[84] AERONET also provides powerful validation for ANG from direct-sun measurements at multiple wavelengths. When sufficient component and mixture options are available, the MISR algorithm distinguishes three to five groupings in ANG, based on sensitivity analysis and case studies for which we have validation data. The MISR V22 product distinguishes two or three size bins, depending on aerosol type, as well as spherical vs. nonspherical particles and, in some circumstances, about two bins in SSA. But unlike the situation for AOD and ANG, there are too few MISR-AERONET coincident validation data for SSA and particle shape to perform formal statistical assessments. To some extent, expected trends in particle absorption properties and nonspherical AOD fraction are observed, and qualitative assessment is supplemented by previously published case studies for which near-coincident field observations were obtained [e.g., Schmid et al., 2003; Kahn et al., 2004, 2009b; Redemann et al., 2005; Reidmiller et al., 2006]. On the basis of the validation study results, specific algorithm upgrades are proposed, and they are summarized in section 5; the MISR team is addressing each of them, such as modifications to the component particle optical models and mixtures to maximize particle type discrimination.

[85] This paper provides formal validation of the MISR V22 aerosol product. As with any remote sensing measurements, there are strengths and limitations. Here we have identified the key issues and traced them to specific retrieval

conditions, information essential for applying and interpreting the data appropriately. Care must be taken with MISR AOD values at the extremes, when the midvisible AOD is likely to be  $>0.5$  and when it is expected to be very small ( $<0.025$ ). The impact of variability on retrieved AOD, especially within aerosol plumes, of bright-water surfaces, and in broken-cloud situations, should also be considered. Sensitivity to particle microphysical properties is diminished for midvisible AOD below about 0.15 or 0.2.

[86] Taking these caveats into account, the MISR-retrieved AOD over water, land, and bright surfaces is used to study zonal mean aerosol short-wave forcing [Kim and Ramanathan, 2008; Kishcha et al., 2009] as well as regional long-wave forcing [Zhang and Christopher, 2003]. The MISR aerosol product has also been used to monitor dust plume evolution [Kalashnikova and Kahn, 2008] and air quality [Liu et al., 2007a, 2007b; van Donkelaar et al., 2010], to map aerosol air-mass type evolution [Dey and Di Girolamo, 2010], and to validate aerosol transport model AOD simulations [Kinne et al., 2006; Yu et al., 2006]. Additional information helpful for applying the MISR aerosol product is given by Kahn et al. [2009a] and in the MISR Data Quality Statements available online ([http://eosweb.larc.nasa.gov/PRODOCS/misr/table\\_misr.html](http://eosweb.larc.nasa.gov/PRODOCS/misr/table_misr.html)).

[87] **Acknowledgments.** We thank our colleagues on the Jet Propulsion Laboratory's MISR instrument team and at the NASA Langley Research Center's Atmospheric Sciences Data Center for their roles in producing the MISR data sets and Susan Paradise for contributions to Figure 4 and related discussion of over-water retrievals. We also thank the AERONET principal investigators for contributing to the global aerosol database, as well as Lorraine Remer and two anonymous reviewers for helpful comments on the manuscript. The work of R. Kahn is supported in part by NASA's Climate and Radiation Research and Analysis Program, under H. Maring, NASA's Atmospheric Composition Program, and the EOS-MISR project.

## References

- Abdou, W. A., D. J. Diner, J. V. Martonchik, C. J. Bruegge, R. A. Kahn, B. J. Gaitley, K. A. Crean, L. A. Remer, and B. Holben (2005), Comparison of coincident MISR and MODIS aerosol optical depths over land and ocean scenes containing AERONET sites, *J. Geophys. Res.*, **110**, D10S07, doi:10.1029/2004JD004693.
- Anderson, T. L., R. L. Charlson, D. M. Winker, J. A. Ogren, and K. Holmen (2003), Mesoscale variations of tropospheric aerosols, *J. Atmos. Sci.*, **60**, 119–136.
- Bi, L., P. Yang, G. W. Kattawar, and R. Kahn (2010), Modeling optical properties of mineral aerosol particles by using non-symmetric hexahedra, *Appl. Opt.*, **49**, 334–342.
- Bond, T. C., and R. W. Bergstrom (2006), Light absorption by carbonaceous particles: An investigative review, *Aerosol Sci. Tech.*, **40**, 27–67.
- Bruegge, C. J., D. J. Diner, R. A. Kahn, N. Chrien, M. C. Helmlinger, B. J. Gaitley, and W. A. Abdou (2007), The MISR radiometric calibration process, *Remote Sens. Environ.*, **107**, 2–11, doi:10.1016/j.rse.2006.07.024.
- Chen, W.-T., R. Kahn, D. Nelson, K. Yau, and J. Seinfeld (2008), Sensitivity of multi-angle imaging to optical and microphysical properties of biomass burning aerosols, *J. Geophys. Res.*, **113**, D10203, doi:10.1029/2007JD009414.
- Chen, Y., Q. Li, R. A. Kahn, J. T. Randerson, and D. J. Diner (2009), Quantifying aerosol direct radiative effect with Multiangle Imaging Spectroradiometer observations: Top-of-atmosphere albedo change by aerosols based on land surface types, *J. Geophys. Res.*, **114**, D02109, doi:10.1029/2008JD010754.
- Christopher, S., and J. Wang (2004), Intercomparison between multi-angle imaging spectroradiometer (MISR) and sunphotometer aerosol optical thickness in dust source regions over China: Implications for satellite aerosol retrievals and radiative forcing calculations, *Tellus, Ser. B*, **56**, 451–456.
- Dey, S., and L. Di Girolamo (2010), A climatology of aerosol optical and microphysical properties over the Indian subcontinent from 9 years



- (2000–2008) of Multiangle Imaging Spectroradiometer (MISR) data, *J. Geophys. Res.*, **115**, D15204, doi:10.1029/2009JD013395.
- Di Girolamo, L., and M. J. Wilson (2003), A first look at band-differenced angular signatures for cloud detection from MISR, *IEEE Trans. Geosci. Remote Sens.*, **41**, 1730–1734.
- Diner, D. J., et al. (1998), Multiangle Imaging Spectroradiometer (MISR) instrument description and experiment overview, *IEEE Trans. Geosci. Remote Sens.*, **36**, 1072–1087.
- Diner, D. J., W. A. Abdou, J. E. Conel, K. A. Crean, B. J. Gaitley, M. Helmlinger, R. A. Kahn, J. V. Martonchik, and S. H. Piliroz (2001), MISR aerosol retrievals over southern Africa during the Safari-2000 dry season campaign, *Geophys. Res. Lett.*, **28**, 3127–3130.
- Diner, D. J., R. A. Kahn, C. J. Bruegge, J. V. Martonchik, W. A. Abdou, B. J. Gaitley, M. C. Helmlinger, O. V. Kalashnikova, and W.-H. Li (2004), Refinements to MISR's radiometric calibration and implications for establishing a climate-quality aerosol observing system, *Proc. SPIE*, **5652**, 57–65.
- Diner, D. J., et al. (2006), *Multi-Angle Imaging Spectroradiometer Level 2 Aerosol Retrieval Algorithm Theoretical Basis, Revision F*, JPL D-11400, Jet Propulsion Laboratory, California Institute of Technology, Pasadena.
- Dubovik, O., and M. D. King (2000), A flexible inversion algorithm for retrieval of aerosol optical properties from Sun and sky radiance measurements, *J. Geophys. Res.*, **105**, 20,673–20,696.
- Dubovik, O., A. Smirnov, B. N. Holben, M. D. King, Y. J. Kaufman, T. F. Eck, and I. Slutsker (2000), Accuracy assessments of aerosol optical properties retrieved from Aerosol Robotic Network (AERONET) Sun and sky radiance measurements, *J. Geophys. Res.*, **105**, 9791–9806.
- Dubovik, O., B. Holben, T. F. Eck, A. Smirnov, Y. J. Kaufman, M. E. King, D. Tanre, and I. Slutsker (2002), Variability of absorption and optical properties of key aerosol types observed in worldwide locations, *J. Atmos. Sci.*, **59**, 590–608.
- Dubovik, O., et al. (2006), Application of spheroid models to account for aerosol particle nonsphericity in remote sensing of desert dust, *J. Geophys. Res.*, **111**, D11208, doi:10.1029/2005JD006619.
- Eck, T. F., B. N. Holben, J. S. Reid, O. Dubovik, A. Smirnov, N. T. O'Neill, I. Slutsker, and S. Kinne (1999), Wavelength dependence of the optical depth of biomass burning, urban, and desert dust aerosols, *J. Geophys. Res.*, **104**, 31,333–31,349.
- Eck, T. F., et al. (2010), Climatological aspects of the optical properties of fine/coarse mode aerosol mixtures, *J. Geophys. Res.*, **115**, D19205, doi:10.1029/2010JD014002.
- Haywood, J., and M. Schulz (2007), Causes of the reduction in uncertainty in the anthropogenic radiative forcing of climate between IPCC (2001) and IPCC (2007), *Geophys. Res. Lett.*, **34**, L20701, doi:10.1029/2007GL030749.
- Holben, B. N., et al. (1998), AERONET—A federated instrument network and data archive for aerosol characterization, *Remote Sens. Environ.*, **66**, 1–16.
- IPCC (2007), *The Physical Science Basis. Contribution of Working Group I to the Fourth Assessment Report of the Intergovernmental Panel on Climate Change*, edited by S. Solomon, D. Qin, H. Manning, Z. Chen, M. Marquis, K. Averyt, M. Tignor, and H. Miller, Cambridge University Press, Cambridge.
- Jiang, X., Y. Liu, B. Yu, and M. Jiang (2007), Comparison of MISR aerosol optical thickness with AERONET measurements in Beijing metropolitan area, *Remote Sens. Environ.*, **107**, 45–53.
- Kahn, R., R. West, D. McDonald, B. Rheingans, and M. I. Mishchenko (1997), Sensitivity of multi-angle remote sensing observations to aerosol sphericity, *J. Geophys. Res.*, **102**, 16,861–16,870.
- Kahn, R., P. Banerjee, D. McDonald, and D. Diner (1998), Sensitivity of multiangle imaging to aerosol optical depth, and to pure-particle size distribution and composition over ocean, *J. Geophys. Res.*, **103**, 32,195–32,213.
- Kahn, R., P. Banerjee, and D. McDonald (2001), The sensitivity of multi-angle imaging to natural mixtures of aerosols over ocean, *J. Geophys. Res.*, **106**, 18,219–18,238.
- Kahn, R., et al. (2004), Environmental snapshots from ACE-Asia, *J. Geophys. Res.*, **109**, D19S14, doi:10.1029/2003JD004339.
- Kahn, R., B. Gaitley, J. Martonchik, D. Diner, K. Crean, and B. Holben (2005a), MISR global aerosol optical depth validation based on two years of coincident AERONET observations, *J. Geophys. Res.*, **110**, D10S04, doi:10.1029/2004JD004706.
- Kahn, R., et al. (2005b), MISR low-light-level calibration, and implications for aerosol retrieval over dark water, *J. Atmos. Sci.*, **62**, 1032–1062.
- Kahn, R. A., M. J. Garay, D. L. Nelson, K. K. Yau, M. A. Bull, B. J. Gaitley, J. V. Martonchik, and R. C. Levy (2007a), Satellite-derived aerosol optical depth over dark water from MISR and MODIS: Comparisons with AERONET and implications for climatological studies, *J. Geophys. Res.*, **112**, D18205, doi:10.1029/2006JD008175.
- Kahn, R. A., W.-H. Li, C. Moroney, D. J. Diner, J. V. Martonchik, and E. Fishbein (2007b), Aerosol source plume physical characteristics from space-based multiangle imaging, *J. Geophys. Res.*, **112**, D11205, doi:10.1029/2006JD007647.
- Kahn, R. A., D. L. Nelson, M. Garay, R. C. Levy, M. A. Bull, J. V. Martonchik, D. J. Diner, S. R. Paradise, E. G. Hansen, and L. A. Remer (2009a), MISR aerosol product attributes, and statistical comparison with MODIS, *IEEE Trans. Geosci. Remote Sens.*, **47**(12), 4095–4114.
- Kahn, R., et al. (2009b), Desert dust aerosol air mass mapping in the western Sahara, using particle properties derived from space-based multi-angle imaging, *Tellus*, **61**, 239–251, doi:10.1111/j.1600-0889.2008.00398.x.
- Kalashnikova, O. V., and R. Kahn (2006), Ability of multiangle remote sensing observations to identify and distinguish mineral dust types: Part 2. Sensitivity over dark water, *J. Geophys. Res.*, **111**, D11207, doi:10.1029/2005JD006756.
- Kalashnikova, O. V., and R. A. Kahn (2008), Mineral dust plume evolution over the Atlantic from combined MISR/MODIS aerosol retrievals, *J. Geophys. Res.*, **113**, D24204, doi:10.1029/2008JD010083.
- Kalashnikova, O. V., R. Kahn, I. N. Sokolik, and W.-H. Li (2005), The ability of multi-angle remote sensing observations to identify and distinguish mineral dust types: Part 1. Optical models and retrievals of optically thick plumes, *J. Geophys. Res.*, **110**, D18S14, doi:10.1029/2004JD004550.
- Kim, D., and V. Ramanathan (2008), Solar radiation budget and radiative forcing due to aerosol and clouds, *J. Geophys. Res.*, **113**, D02203, doi:10.1029/2007JD008434.
- Kinne, S., et al. (2006), An AeroCom initial assessment—Optical properties in aerosol component modules of global models, *Atmos. Chem. Phys.*, **6**, 1815–1834.
- Kishcha, P., B. Starobinets, O. Kalashnikova, C. N. Long, and P. Alpert (2009), Variations of meridional aerosol distribution and solar dimming, *J. Geophys. Res.*, **114**, D10D14, doi:10.1029/2008JD010975.
- Levy, R. C., L. A. Remer, S. Mattoo, E. F. Vermote, and Y. J. Kaufman (2007), Second-generation operational algorithm: Retrieval of aerosol properties over land from inversion of Moderate Resolution Imaging Spectroradiometer spectral reflectance, *J. Geophys. Res.*, **112**, D13211, doi:10.1029/2006JD007811.
- Levy, R. C., L. A. Remer, R. G. Kleidman, S. Mattoo, C. Ichoku, R. Kahn, and T. F. Eck (2010), Global evaluation of the Collection 5 MODIS dark-target aerosol products over land, *Atm. Chem. Phys. Discuss.*, **10**, 14,815–14,873.
- Liu, Y., J. A. Sarnat, B. A. Coull, P. Koutrakis, and D. J. Jacob (2004), Validation of Multiangle Imaging Spectroradiometer (MISR) aerosol optical thickness measurements using Aerosol Robotic Network (AERONET) observations over the contiguous United States, *J. Geophys. Res.*, **109**, D06205, doi:10.1029/2003JD003981.
- Liu, Y., P. Koutrakis, and R. Kahn (2007a), Estimating PM<sub>2.5</sub> component concentrations and size distributions using satellite-retrieved fractional aerosol optical depth: Part 1. Development of methods, *J. Air Waste Manage. Assoc.*, **57**, 1351–1359.
- Liu, Y., P. Koutrakis, R. Kahn, S. Turqueti, and R. M. Yantosca (2007b), Estimating PM<sub>2.5</sub> component concentrations and size distributions using satellite-retrieved fractional aerosol optical depth: Part 2. A case study, *J. Air Waste Manage. Assoc.*, **57**, 1360–1369.
- Martonchik, J. V., D. J. Diner, R. Kahn, M. M. Verstraete, B. Pinty, H. R. Gordon, and T. P. Ackerman (1998), Techniques for the retrieval of aerosol properties over land and ocean using multiangle imaging, *IEEE Trans. Geosci. Remote Sens.*, **36**, 1212–1227.
- Martonchik, J. V., D. J. Diner, K. Crean, and M. Bull (2002), Regional aerosol retrieval results from MISR, *IEEE Trans. Geosci. Remote Sens.*, **40**, 1520–1531.
- Martonchik, J. V., D. J. Diner, R. A. Kahn, B. J. Gaitley, and B. N. Holben (2004), Comparison of MISR and AERONET aerosol optical depths over desert sites, *Geophys. Res. Lett.*, **31**, L16102, doi:10.1029/2004GL019807.
- Martonchik, J. V., R. A. Kahn, and D. J. Diner (2009), Retrieval of aerosol properties over land using MISR observations, in *Satellite Aerosol Remote Sensing Over Land*, edited by A. Kokhanovsky, Springer, Berlin.
- Pierce, J. R., R. A. Kahn, M. R. Davis, and J. M. Comstock (2010), Detecting thin cirrus in MISR aerosol retrievals, *J. Geophys. Res.*, **115**, D08201, doi:10.1029/2009JD013019.
- Press, W. H., S. A. Teukolsky, W. T. Vetterling, and B. P. Flannery (2007), *Numerical Recipes*, 3rd ed., 1235 pp., Cambridge University Press, Cambridge.
- Redemann, J., B. Schmid, J. A. Eilers, R. Kahn, R. C. Levy, P. B. Russell, J. M. Livingston, P. V. Hobbs, W. L. Smith Jr., and B. N. Holben (2005), Suborbital measurements of spectral aerosol optical depth and its variability

- ity at sub-satellite-grid scales in support of CLAMS, 2001, *J. Atmos. Sci.*, **62**(4), 993–1007, doi:10.1175/JAS3387.1.
- Redemann, J., Q. Zhang, B. Schmid, P. B. Russell, J. M. Livingston, H. Jonsson, and L. A. Remer (2006), Assessment of MODIS-derived visible and near-IR aerosol optical properties and their spatial variability in the presence of mineral dust, *Geophys. Res. Lett.*, **33**, L18814, doi:10.1029/2006GL026626.
- Reidmiller, D. R., P. V. Hobbs, and R. Kahn (2006), Aerosol optical properties and particle size distributions on the east coast of the United States, derived from airborne in situ and remote sensing measurements, *J. Atmos. Sci.*, **63**, 785–814.
- Remer, L. A., et al. (2005), The MODIS aerosol algorithm, products, and validation, *J. Atmos. Sci.*, **62**, 947–973.
- Remer, L. A., et al. (2008), Global aerosol climatology from the MODIS satellite sensors, *J. Geophys. Res.*, **113**, D14S07, doi:10.1029/2007JD009661.
- Schladits, A., T. Muller, A. Massling, N. Kaaden, K. Kandler, and A. Wiedensohler (2009), In situ measurements of optical properties at Tin-fou (Morocco) during the Saharan mineral dust experiment, SAMUM 2006, *Tellus*, **61B**, 64–78, doi:10.1111/j.1600-0889.2008.00397.x.
- Schmid, B., et al. (2003), Coordinated airborne, spaceborne, and ground-based measurements of massive, thick aerosol layers during the dry season in southern Africa, *J. Geophys. Res.*, **108**(D13), 8496, doi:10.1029/2002JD002297.
- Schuster, G. L., O. Dubovik, and B. N. Holben (2006), Angstrom exponent and bimodal aerosol size distributions, *J. Geophys. Res.*, **111**, D07207, doi:10.1029/2005JD006328.
- Smirnov, A., B. N. Holben, T. F. Eck, O. Dubovik, and I. Slutsker (2000), Cloud screening and quality control algorithms for the AERONET database, *Remote Sens. Environ.*, **73**, 337–349.
- Smirnov, A., et al. (2009), Maritime Aerosol Network as a component of Aerosol Robotic Network, *J. Geophys. Res.*, **114**, D06204, doi:10.1029/2008JD011257.
- van Donkelaar, A., R. V. Martin, M. Brauer, R. Kahn, R. Levy, C. Verduzco, and P. Villeneuve (2010), Global estimates of average ground-level fine particulate matter concentrations from satellite-based aerosol optical depth, *Environ. Health Perspect.*, **118**, 847–855.
- Yu, H., et al. (2006), A review of measurement-based assessment of aerosol direct radiative effect and forcing, *Atmos. Chem. Phys.*, **6**, 613–666.
- Zhang, J., and S. Christopher (2003), Longwave radiative forcing of Saharan dust aerosols estimated from MODIS, MISR, and CERES observations on Terra, *Geophys. Res. Lett.*, **30**(23), 2188, doi:10.1029/2003GL018479.
- Zhao, G., and L. Di Girolamo (2004), A cloud fraction versus view angle technique for automatic in-scene evaluation of the MISR cloud mask, *J. Appl. Meteorol.*, **43**(6), 860–869.
- Zhao, G., L. Di Girolamo, S. Dey, A. L. Jones, and M. Bull (2009), Examination of direct cumulus contamination on MISR-retrieved aerosol optical depth and angstrom coefficient over ocean, *Geophys. Res. Lett.*, **36**, L13811, doi:10.1029/2009GL038549.
- D. J. Diner and B. J. Gaitley, Jet Propulsion Laboratory, California Institute of Technology, 4800 Oak Grove Drive, Pasadena, CA 91109, USA.
- T. F. Eck, Goddard Earth Sciences and Technology Center, University of Maryland Baltimore County, 5523 Research Park Dr., Ste. 320, Baltimore, MD 21228, USA.
- M. J. Garay, Raytheon Company, 299 North Euclid Avenue, Suite 500, Pasadena, CA 91101, USA.
- B. N. Holben and R. A. Kahn, Laboratory for Atmospheres, NASA Goddard Space Flight Center, Greenbelt, MD 20771, USA. (ralph.kahn@nasa.gov)
- A. Smirnov, Sigma Space Corporation, 4400 Lottsford Vista Road, Lanham, MD 20706, USA.